Large Eddy Simulation of separated flow to investigate heat transfer characteristics in an asymmetric diffuser subjected to constant wall heat flux

Amin Bekhradinasab[a], Jafar Al-Zaili[b], Shidvash Vakilipour[a,*]

[a] *Faculty of New Sciences and Technologies, University of Tehran, North Kargar, Tehran, Iran*
[b] *Department of Mechanical Engineering & Aeronautics, City, University of London, Northampton Square, London, EC1V 0HB, UK*

Abstract

In the present study, heat transfer characteristics of an asymmetric diffuser with separated flow has been studied. The flow separation is triggered due to wall expansion in two directions. Large Eddy Simulation (LES) approach is adopted to solve the turbulent separated flow and heat transfer in such diffuser at Reynolds number of 10000. For this purpose, a finite volume solver is extended in the OpenFOAM framework to solve the energy equation for incompressible flow. The extended solver has been adjusted to deal with backscatter phenomena and to prevent non-physical heat transfer results and numerical instability. An appropriate grid resolution is employed to perform LES calculations and predict the characteristics of the heat transfer within the separated flow. The numerical results are validated against measurements and Direct Numerical Simulation (DNS) results. The present study showed that the low mean velocity and turbulent kinetic energy (TKE) in a separated flow region are responsible for generating high temperature hot spots resulted from significant reduction of heat transfer from the walls. It has been observed that the heat transfer from the wall is increased slightly before the flow reattachment region. The applicability of the Reynolds analogy in the separated flow zone for this problem has been examined. Moreover, the analysis of the computational performance showed that increasing the number of computational cells can improve, to certain extent, the convergence rate of the solver and therefor, reduced the computation cost.

Keywords: Large Eddy Simulation, Separated flow, Heat transfer, Asymmetric diffuser, Turbulent flow, OpenFOAM.

1. Introduction

Flow separation and heat transfer are among the most studied fluid flow problems that have received much attention both in academic and applied engineering. One of the main factors to cause flow separation

*Corresponding author
Email address: vakilipour@ut.ac.ir (Shidvash Vakilipour)

is the existence of an adverse pressure gradient. Adverse pressure and comparatively separation can be observed in some engineering equipment. In some of them, heat transfer also plays an important role, such as Turbine blades [1–3], turbines [4], compressors, diffusers, heat exchangers [5, 6], and combustion chambers [7, 8] are some of the devices including heat transfer where the flow separation is possible. Heat transfer inside the diffusers is also important in micro-gas turbines, significantly influencing the device's thermal and overall efficiencies. Therefore, the researchers have worked on heat transfer inside a micro-gas turbine and its impact on performance [9–12]. Computational fluid dynamics is one of the most favourite methods that scientists and designers use to study fluid flow and heat transfer from micro [13, 14] to macro-scale, including separation phenomena. To do this, one needs to look at the boundary layer and flow characteristics alongside the wall, which is one of the most costly and challenging problems in computational fluid dynamics [15].

Cherry et al. [16] empirically investigated the problem of three-dimensional separation with turbulent flow in two diffusers. Since the returned separated flow is a severe numerical simulation challenge, they designed these diffusers as the general model of the three-dimensional separated flow that can be used directly compared to numerical simulation. The Reynolds number of both diffusers based on the inlet channel height was set to 10,000, and water was used as the operating fluid. The diffusers investigated by Cherry et al. [16] are standard cases for flow separation and its related phenomena. The heat transfer can also be a general and standard case for all three-dimensional internal flow devices, with the separation of flow and heat transferworks in Mach numbers below 0.3. The elements used to simulate this problem - such as simulation approach, discretization scheme, solution algorithm, and mesh quality - are shown to be essential for simulation of transient separation successfully [17].

Ohlsson et al. [18] investigated the flow in the Diffuser 1 studied by Cherry et al. [16] (Cherry diffuser) by DNS performed at Reynolds 10,000 on a mesh with approximate cell number of 220 million by a super-computer with 32,768 cores. The results are accurate in which they can be used to validate other numerical studies in this geometry. Jakirlić et al. [19] used a recently proposed hybrid LES and Reynolds-Averaged Navier-Stokes (RANS) method and an LES method along with the dynamic Smagorinsky SubGrid-Scale (SGS) model to simulate the flow in the Cherry diffuser, which developed some excellent results. Abe and Ohtsuka [20] compared an LES approach and a combination of LES and RANS in simulating a three-dimensional diffuser flow. The results showed that the hybrid method provides a more accurate response in a coarse grid than the LES. On the coarse grid, LES has not shown the separation correctly, but the simulation results are comparable with the experimental results in the hybrid method. Abe [21] investigated an SGS stress anisotropy modeling in complex turbulent flow fields. Abe took into account several geometries, which Cherry diffuser was one of them. The SGS model was constructed by combining an isotropic linear eddy-viscosity model with an additional anisotropic term to prevent the transfer of undesirable energy between the grid-scale and SGS parts. One of the crucial points of this study was to show that using this model does not affect the simulation stability. The results of this study were in agreement with the DNS results and experimental measurements.

Togun et al. [22] experimentally investigated the effect of flow separation from a backward step geometry on heat transfer. Oon et al. [23] studied the same geometry in the Fluent software with RANS k-ϵ method in different Reynolds numbers and discussed the effects of separation on heat transfer. Togun et al. [24] investigated the heat transfer characteristics of nano-fluid flowing in an annular pipe at different Reynolds numbers. They showed that surface heat transfer increased with increasing of either nano particles volume fraction or Reynolds number. They also showed that the flow separation affect the heat transfer coefficient and the highest local heat transfer coefficient is estimated to be in the re-attachment region. Durbin et al. [25] simulated the effect of the inlet channel aspect ratio on flow separation in the diffuser by LES and Delayed Detached Eddy Simulation (DDES) approaches. Schneider et al. [26] investigated k-ω RANS and LES approach with a specific type of wall-functions which could be switched off near the separation regions. They reported that the RANS method failed to produce acceptable results, but the LES approach with standard Smagorinsky subgrid-scale model and van Driest damping produced acceptable results. Most of the RANS methods failed to predict flow separation within a diffuser as discussed in ERCOFTAC [27] workshops. Other papers, such as [25] and [26], have emphasized that the RANS methods failed to predict both the extent and location of the separation. Weatheritt and Sandberg [28] used machine learning to improve the relationships between the stress tensors in the RANS and hybrid models. Instead of looking for a universal framework for all geometries, machine learning obtained a class of stress-strain relationships suitable for flows with simillar topology. The Cherry diffuser was one of the geometries studied using a hybrid simulation method. Yin and Durbin [29] improved the adaptive-DES method proposed by Yin et al. [30], which could be converted to wall-resolved eddy simulation with a suitable grid resolution. They also applied this method to the Jeyapaul diffuser series [31] diffuser seriesbased on the Cherry diffuser. Since RANS methods used previously did not provide acceptable results, Jakirlić and Maduta [32] investigated the ability of RANS to capture turbulence unsteadiness. They investigated a new Sensitized RANS based formulation on different cases. One of them was the Cherry diffuser. The results showed a significant improvement over the RANS methods used before.

This paper aims to study the heat transfer in the three-dimensional separated flow to understand the effects of separation on the heat transfer characteristics. A three-dimensional diffuser, specifically designed for comparison with CFD results, is used to validate the simulation results of the current study. The first objective of this paper is to obtain velocity field profiles in the diffuser. The LES approach and the dynamic Smagorinsky SGS are employed to simulate the flow field in this diffuser. Alongside the velocity and pressure fields, the equation for conservation of energy is solved to obtain the turbulent temperature field in the simulation. OpenFOAM (Open-source Field Operation And Manipulation) is an open source computational fluid dynamics software that is used as a framework to solve the flow and temperature equations. For the purpose of this study, pimpleFoam is extended in which prevents non-physical results for backscatter phenomena. The temperature field in a channel is simulated using the extended solver, and the results are compared and validated with the DNS results of Kim and Moin [33]. Also, a simulation of backward-facing step is performed to assess suitability of the extended solver in turbulent separated flow regimes and the thermal result is validated against the DNS result of Niemann and Fröhlich [34] and the LES prediction of Avancha and Pletcher [35]. The temperature field is added to the diffuser flow, and the effect of separation on the temperature profiles and heat transfer coefficient was investigated and reported.

2. Computational method

In most thermo-fluid applications, DNS simulations of turbulence are costly and need considerable computational resources. On other hand, RANS simulations cannot provide accurate results in complex CFD simulations. For such simulations, LES approach is widely used as it provides more accurate results than RANS with less computational resources than DNS. LES resolves large scales of flow, which control turbulent diffusion of momentum or heat. LES uses a filter function ($\bar{G}$) to purge the turbulence scales smaller than the grid mesh size. The filtered field is defined for a quantity f as [36]

$$\bar{f}\left(x,t\right) = \int f\left(y,t\right)\bar{G}\left(x-y\right)dy = \int f\left(x-y,t\right)\bar{G}\left(y\right)dy \tag{1}$$

The filtered continuity equation for an incompressible flow has the same form of the original equation as follows

$$\frac{\partial \bar{u}_i}{\partial x_i} = 0. \tag{2}$$

The unsteady Navier-Stokes equations for incompressible flow of a Newtonian fluid are given by

$$\frac{\partial u_i}{\partial t} + \frac{\partial}{\partial x_j}\left(u_i u_j\right) = -\frac{1}{\rho}\frac{\partial p}{\partial x_i} + \frac{\partial}{\partial x_j}\left[\nu\left(\frac{\partial u_i}{\partial x_j} + \frac{\partial u_j}{\partial x_i}\right)\right] \tag{3}$$

where t, u, ρ, p, and ν is time, velocity, density, pressure, and kinematic viscosity, respectively. Applying the LES filter on Navier-Stokes equations gives:

$$\frac{\partial \bar{u}_i}{\partial t} + \frac{\partial}{\partial x_j}\left(\bar{u}_i \bar{u}_j\right) = -\frac{1}{\rho}\frac{\partial \bar{p}}{\partial x_i} + \frac{\partial}{\partial x_j}\left[\nu\left(\frac{\partial \bar{u}_i}{\partial x_j} + \frac{\partial \bar{u}_j}{\partial x_i}\right) + \mathbb{T}_{ij}\right] \tag{4}$$

where the subgrid-scale tensor $\mathbb{T}_{ij}$ is given by

$$\mathbb{T}_{ij} = \bar{u}_i\bar{u}_j - \overline{u_i u_j}. \tag{5}$$

The continuity equation remains unchanged after filtering, but the filtered momentum equations involve an additional term compared to the original equation called subgrid-scale tensor. Subgrid-scale tensor must be modelled to close the system of equation. The closure problem arises from implementation of the averaging process on the nonlinear Navier-Stokes equations. This tensor is also physically necessary for energy balance and applying subgrid-scale effects. The modelled scales are those with length and time scales lower than the spatial and temporal filter width, respectively. In most of the cases, the subgrid-scale tensors are expressed in terms of eddy viscosity, ν_t,

$$\mathbb{T}_{ij} = 2\nu_t \bar{S}_{ij} + \frac{1}{3}\mathbb{T}_{ll}\delta_{ij} \tag{6}$$

where

$$\bar{S}_{ij} = \frac{1}{2}\left(\frac{\partial \bar{u}_i}{\partial x_j} + \frac{\partial \bar{u}_j}{\partial x_i}\right) \tag{7}$$

is the filtered-field strain rate tensor. Therefore, the filtered Navier-Stokes equations yield

$$\frac{\partial \bar{u}_i}{\partial t} + \bar{u}_j \frac{\partial \bar{u}_i}{\partial x_j} = -\frac{1}{\rho}\frac{\partial \bar{P}}{\partial x_i} + 2\frac{\partial}{\partial x_j}\left[(\nu + \nu_t)\,\bar{S}_{ij}\right] \tag{8}$$

where the modified pressure is $\bar{P} = \bar{p} - \left(\frac{1}{3}\right)\rho\mathbb{T}_{ll}$. In the LES method, different models have been developed for modelling eddy viscosity. These SGS models are responsible for the high frequency and small length scale eddies, which are mostly dissipating scales. The SGS models are used to perform the effects of unresolved small scale fluid motions. This effect can be seen as the modeled turbulent kinetic energy, which is added to the resolved turbulent kinetic energy to accurately predict the total turbulent kinetic energy of the flow. Smagorinsky [37] proposed the following equation to calculate the eddy viscosity

$$\nu_t = (C_s \Delta x)^2 \left|\bar{S}\right| \tag{9}$$

where $\left|\bar{S}\right| = \left(2\bar{S}_{ij}\bar{S}_{ij}\right)^{1/2}$ and C_s and Δx are the Smagorinsky constant and filter width, respectively. In this study dynamic procedure was used, which developed by Germano et al. [38] to calculate C_s dynamically and based on a test filter $(\widetilde{\Delta x})$. The test filter is larger than the primary filter and it is common to assume it equal to $2\Delta x$. If the test filter is applied to the filtered Navier-Stokes equations, the subgrid-scale tensor of the field $\tilde{\bar{u}}$ that must be modelled becomes

$$\mathcal{T}_{ij} = \tilde{\bar{u}}_i \tilde{\bar{u}}_j - \widetilde{\overline{u_i u_j}} \tag{10}$$

and the resolved turbulent stress corresponding to the test filter applied to the field $\bar{u}$ is

$$\mathcal{L}_{ij} = \tilde{\bar{u}}_i \tilde{\bar{u}}_j - \widetilde{\bar{u}_i \bar{u}_j} \tag{11}$$

where $\mathcal{L}_{ij}$ is the Leonard's tensor. Considering Eqs 5, 10, and 11, the Germano's identity is given in the form

$$\mathcal{L}_{ij} = \mathcal{T}_{ij} - \widetilde{\mathbb{T}}_{ij} \tag{12}$$

where $\widetilde{\mathbb{T}}_{ij}$ is obtained by applying the test filter to Eq. 5. The Smagorinsky's model expression for the subgrid-scale tensor is applied to $\widetilde{\mathbb{T}}_{ij}$ to find that

$$\widetilde{\mathbb{T}}_{ij} - \frac{1}{3}\widetilde{\mathbb{T}}_{ll}\delta_{ij} = 2\widetilde{A_{ij}C} \tag{13}$$

where $C = C_s^2$ and

$$A_{ij} = (\Delta x)^2 \left|\bar{S}\right| \bar{S}_{ij}. \tag{14}$$

$\mathcal{T}_{ij}$ is determined by the Smagorinsky model, which in return gives

$$\mathcal{T}_{ij} - \frac{1}{3}\mathcal{T}_{ll}\delta_{ij} = 2B_{ij}C \tag{15}$$

with

$$B_{ij} = (2\Delta x)^2 \left|\tilde{\bar{S}}\right| \tilde{\bar{S}}_{ij}. \tag{16}$$

By subtracting Eq. 13 from Eq. 15 one can find that

$$\mathcal{L}_{ij} - \frac{1}{3}\mathcal{L}_{ll}\delta_{ij} = 2B_{ij}C - 2\widetilde{A_{ij}C}. \tag{17}$$

Assuming that C is unchanged within the volume of the test filter Eq. 17 becomes [19]

$$\mathcal{L}_{ij} - \frac{1}{3}\mathcal{L}_{ll}\delta_{ij} = 2CM_{ij} \tag{18}$$

where

$$M_{ij} = B_{ij} - \widetilde{A_{ij}}. \tag{19}$$

Equation 18 represents five independent equations for one variable C, and thus the problem is over-determined in its current form. Lilly [39] chose to determine the value of C in Eq. 18 by minimizing an error equation using a least-squares method results in:

$$C = \frac{1}{2}\frac{\mathcal{L}_{ij}M_{ij}}{M_{ij}^2}. \tag{20}$$

To avoid excessively large values of C, the numerators and denominators of Eq. 20 is averaged over space [40]. As a common practice, a limiter is applied to the calculations of ν_t to ensure that the effective viscosity is non-negative. Negative values of the effective viscosity are removed by applying the SGS viscosity limiter in form of $\nu_t = max\left(-v, \nu_t\right)$, to avoid non-physical behaviour and numerical instabilities. The pimpleFoam has been extended to solve incompressible flow energy equation for LES calculations. It has been adjusted to solve the problem of backscatter phenomenon in heat transfer calculation. The energy balance equation for an incompressible flow for the temperature field, T, is expressed by

$$\frac{\partial T}{\partial t} + \frac{\partial}{\partial x_j}\left(u_j T\right) = \frac{\partial}{\partial x_j}\left(\alpha \frac{\partial T}{\partial x_j}\right) \tag{21}$$

where α is the thermal diffusivity coefficient. For LES turbulence simulation and similar to the approach taken for the flow equations, the filtered version of the energy equation becomes

$$\frac{\partial \bar{T}}{\partial t} + \bar{u}_j \frac{\partial \bar{T}}{\partial x_j} = \frac{\partial}{\partial x_j}\left(\alpha_{eff} \frac{\partial \bar{T}}{\partial x_j}\right) \tag{22}$$

where, $\bar{T}$ is the filtered temperature field and $\alpha_{eff} = \alpha + \alpha_t$. The subgrid thermal diffusivity, α_t, is calculated from the ratio of turbulence viscosity to turbulent Prandtl number. The latter is a dimensionless parameter that is a characteristic of the flow regime, not a fluid property. The turbulent Prandtl number is considered commonly 0.85 in a turbulence modelling. Equation 23 shows the dimensionless temperature in which T_{in} is the inlet temperature, n is the coordinate normal to the wall, and H is the inlet cross-section height.

$$\theta = \frac{2\,(T - T_{in})}{\left(\frac{\partial T}{\partial n}\right)_{wall} \mathrm{H}} \tag{23}$$

An expression for the Nusselt number is given by Eq. 24 where q is the heat flux from the wall and k is the thermal conductivity of the fluid.

$$\mathrm{Nu} = \frac{q\,\mathrm{H}}{2\,(T_{wall} - T_{in})\,k} \tag{24}$$

The generation of negative subgrid viscosity in dynamic models due to energy return causes non-physical heat transfer behaviour. Energy transfer from smaller to larger eddy, the backscatter, is due to induction of eddies so that two small eddies may merge and increase their energy level. Piomelli et al. [41] emphasized that this phenomenon should not be overlooked in LES as it may reduce the accuracy of the simulations. The effects of SGS viscosity in the unstable regions, with a negative value of SGS viscosity, can be ignored. This is due to the fact that most of the LES kinetic energy is already resolved in these regions [42]. A limiter has been applied for α_{eff}, similar to the one used for the turbulent viscosity, to avoid any non-positive values for the effective diffusivity. Negative (or zero) effective diffusivity implies that heat is transferred from the cooler fluid to the warmer wall. In the case of zero effective diffusivity, the heat transfer between two regions with different temperatures is zero. Both of these cases are non-physical and should be avoided in the simulations. For fluids with $Pr < Pr_t$, the SGS viscosity limiter will be sufficient to satisfy the condition of $\alpha_{eff} > 0$. However, for fluids, such as water, where $Pr > Pr_t$, a separate limiter is necessary to ensure that the effective diffusivity is strictly positive. A limiter has been implemented in extended solver in form of $\alpha_t = \max(\alpha_t, 0)$. OpenFOAM incompressible flow solver, pimpleFoam, was used in the current study to perform the LES flow simulations. This solver is based on a combination of SIMPLE (Semi-Implicit Method for Pressure Linked Equations) and PISO (Pressure-Implicit with Splitting of Operators) numerical schemes. The pimpleFoam solver was operated in PISO mode to enable the unsteady flow calculations needed for the LES simulations. A second-order backward scheme was used for time derivatives. The second order and Gaussian integration was used for the gradient and Laplacian terms, respectively.

3. Problem description and the test cases

The geometric details of the studied diffuser and its dimensions are shown in Fig. 1, where H is the inlet cross-section height. The inlet cross-section width (W) and the length of zone III (L) are used to nondimensionalize the coordinates in z and x directions. The values of H, W, and L are taken equal to

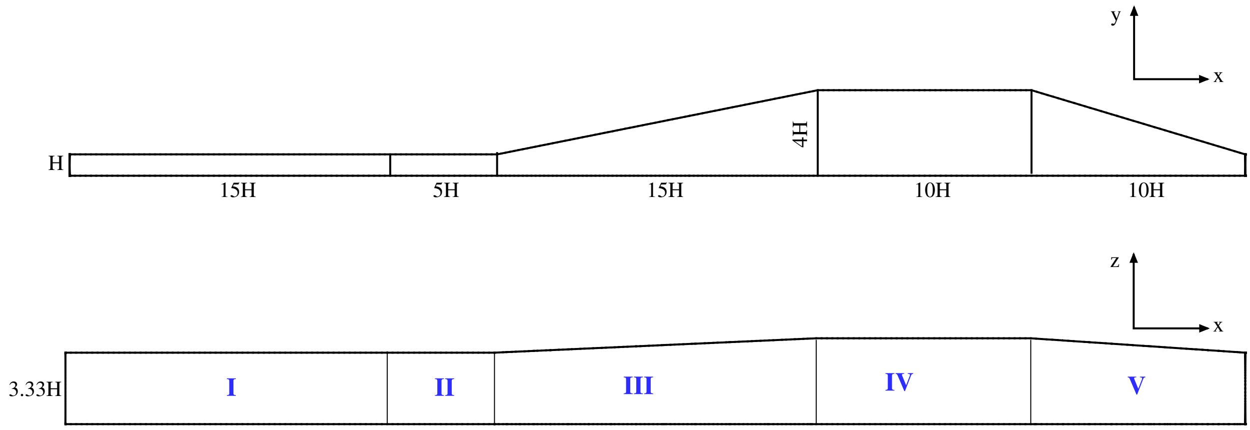

Figure 1: Description of the diffuser geometry, dimensions, and computational zones represented from side (up) and up (bottom) views.

1 cm, 3.33 cm, and 15 cm, respectively, as specified in the experimental setup of Cherry et al. [16]. The curvature of the opening, the interface between zone II and zone III, was replaced by a sharp edge to simplify the geometry. This will result in a minor separation at the beginning of the diffuser's openings, which can be safely neglected [26]. The effect of this minor separation will be discussed in the results section. For simplicity, the outlet of the domain (end of zone V) was considered as a rectangular section, while in the experimental setup of Cherry et al. [16] the cross section was circular. Moreover, the length of the channel after the main part of the diffuser was shortened from 12.5 H to 10 H to reduce the computational cost in a less critical part of the domain. It has been demonstrated by Durbin et al. [25] that the last modification has an insignificant effect on the flow characteristics of the diffuser (zone III).

In the experimental work of Cherry et al. [16], the inlet of the diffuser was a fully developed turbulent flow. The boundary conditions in zone I were set to ensure a fully developed turbulent flow in the inlet of the diffuser. Unless a specialized boundary condition is implemented for zone I, the length of this zone should be nearly 63H to achieve a fully developed flow [18]. The mapped method introduced by Baba-Ahmadi and Tabor [43] have been applied in zone I to achieve a fully developed flow by a much shorter length of 15H. Montorfano et al. [44] and Jakirlić et al. [19] have used successfully this boundary condition for similar cases. Implementation of this boundary condition resulted in considerable saving in the computation costs. In this method, the flow properties, except the pressure, are mapped from the output of the channel to its input. Jakirlić et al. [19] have noted that over-shortening, below 5H, of the channel, causes inaccuracy in capturing the flow structure. The length of 15H seems a conservative choice, which has proved to generate a fully developed flow in zone I as intended. Non-slip boundary condition was applied on all walls in the domain, and a zero-gradient velocity boundary condition and fixed-value pressure were used in the outlet.

Table 1: Grid specifications for the computational Cases A, B, and C: grid distribution of diffuser zones in x direction, n_I to n_V, grid distribution in y and z directions, n_y and n_z, the highest computational grid spacing in x and z directions and the total number of grid.

Case	n_I	n_II	n_III	n_IV	n_V	n_y	n_z	$\Delta\mathrm{x}^+_\mathrm{max}$	$\Delta\mathrm{z}^+_\mathrm{max}$	Total number of grid
Case A	60	20	75	40	40	100	100	68	96	1,750,000
Case B	120	40	150	90	40	100	100	46	98	3,200,000
Case C	120	40	150	90	40	94	169	42	12	5,083,520

For the temperature calculations, the inlet temperature in zone I was set to 293 K, zero gradient temperature boundary condition was applied to the outlet of the domain. The walls of zone I and the sidewalls in the other zones are treated as adiabatic. In contrast, on the upper and lower walls of the main domain, a fixed heat flux of 138 kW/m^2 was arbitrarily assumed, which is equivalent to a fixed wall temperature gradient of 2.3$\times$10^5 K/m. These values are set to ensure that there is a significant variation in the temperature field.

The ratio of the total length of the domain to the flow inlet velocity indicates approximately the time that the flow needs to pass the domain, the so-called flow-through time (τ). It usually takes between 5τ to 10τ for the flow field to stabilize and for the velocity profiles to take shape in LES simulations. Following a common practice in LES simulations, the Courant number was set to 0.3 for all cases. The simulations required about 10τ to achieve a fully developed flow in the development channel (zone I). The simulations then were allowed a further 8τ to obtain statistically steady flow in the primary domain (zone II, III, IV and V). The time averaging has been performed over 16τ of the primary domain to find the time-averaged properties of the flow.

The details of the spatial spacing in the three directions and total number of grid for the studied cases are given in Table 1. The total number of grids does not contain the zone I as this zone was used just to provide a fully developed flow, and that is not a part of the main geometry. For all cases, the spacing in the normal and spanwise direction was kept the same for all five zones of the computational domain. While the streamwise spacing varies for the different zones with the target to keep $\Delta\mathrm{x}^+_{max}$ below 50 in diffuser zone (zone III). The dimensionless normal grid spacing $\Delta\mathrm{y}^+_{max}$ should be kept below 1 on the wall. The dimensionless spanwise grid spacing $\Delta\mathrm{x}^+_{max}$ should not exceed 30 in the near wall as Rezaeiravesh and Liefvendahl [45] suggested for accuracy of the LES calculations. Case A and B were used initially to estimate the values of dimensionless turbulent grid spacing in the domain. Case C was chosen to respect the above mentioned constraints on the grid spacing. In Case B, the number of grid points in the flow direction was increased compared to Case A. These values are in line with those suggested by Rezaeiravesh and Liefvendahl [45] for high-quality LES simulation in channels.

Figure 2 shows the variation and the details of the dimensionless wall distance $\Delta\mathrm{y}^+_1$ where the value of $\Delta\mathrm{y}^+_1$ was kept below 1 in all cases. However, in Case A, the streamwise spacing was above 50 in some

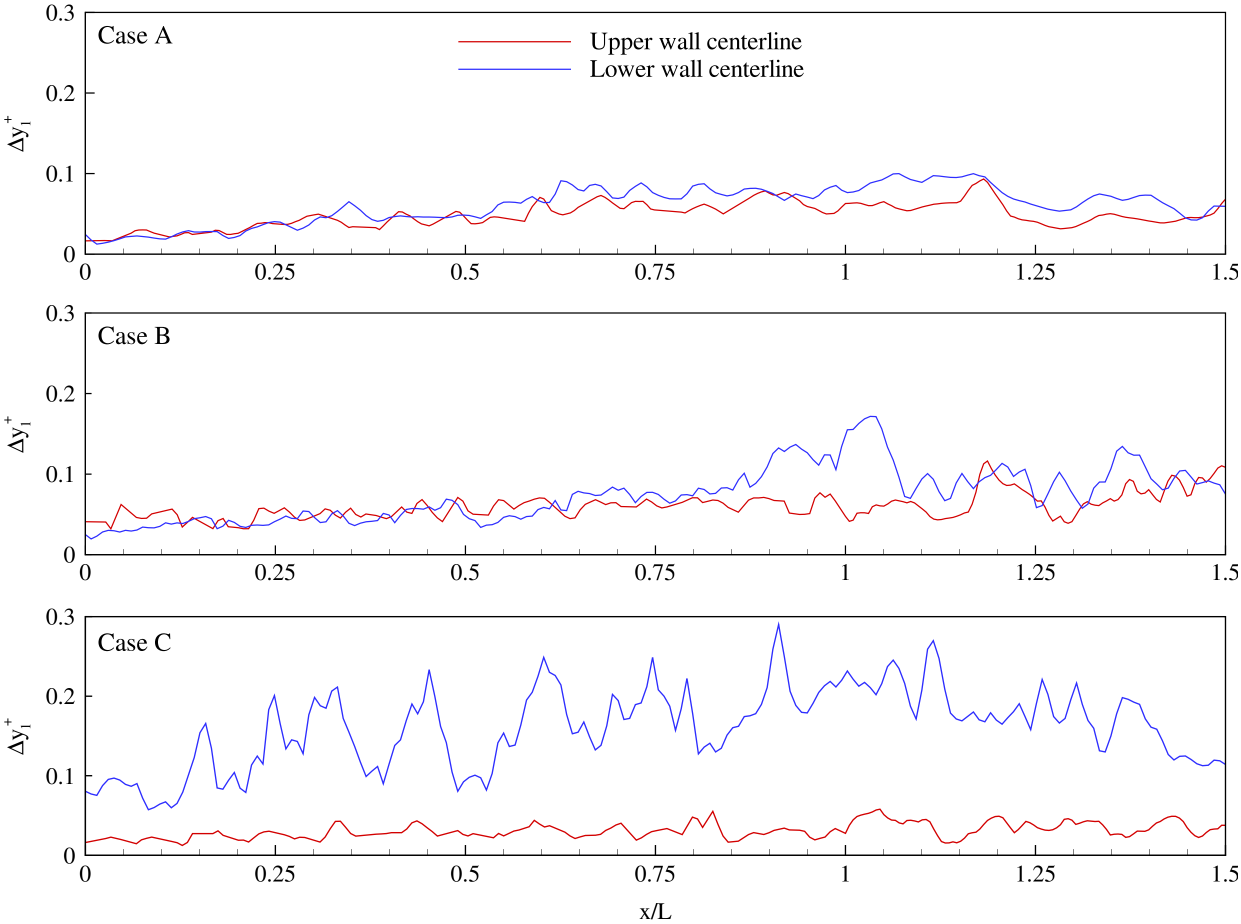

Figure 2: First-layer grid resolution, Δy_1^+, along the center-line of the diffuser upper and lower walls at z/W=1/4, 1/2, and 3/4 in zones III and IV.

regions but below this limit for Case B and Case C.

4. Results and discussion

LES calculations have been performed for three cases A, B and C, described in the previous section. The modelling specifications and the numerical schemes have been detailed in Section 2. In this section, the averaged velocity field, pressure, and turbulence intensity have been extracted from the LES calculations and compared with DNS results of Ohlsson et al. [18] and measurements of Cherry et al. [16]. The ratio of the resolved to total TKE, i.e. $\mathrm{TKE_{res}}/\mathrm{TKE_{tot}}$, and Power Spectral Density (PSD) have been used to assess the LES results qualitatively. It should be mentioned that the experimental data provided by Cherry et al. [16] are out of the original geometric dimensions. Therefore, the geometry has been scaled for reasonable comparisons with the provided measurements.

Figure 3 shows the velocity profiles calculated on Cases A, B, and C on x-y planes at z/W = 1/4, 1/2, and 3/4. A flow separation was predicted on the diffuser upper wall and corners in Cases C and B, respectively. On the other hand, this was not observed in the numerical results achieved by Case A. In Case A, the velocity profile agrees with the experimental results at the diffuser entrance. However, the discrepancy between its results and the measurements increases as flow advances in the diffuser. The velocity profiles of Case B shows better agreement with the experimental data where a flow separation prediction was improved in the upper corners of the side-walls. However, the flow separation at the center of the upper wall was not resolved in this case. Hence, the grid resolution was increased in the spanwise direction for Case C in comparison to Case B. The flow recirculation lengths have been calculated from present numerical results of Case C at three planes with z/W=1/4, 1/2, and 3/4. The relative differences with respect to data of Cherry et al. [16]. are 12.77 %, 3.11 %, and 14.89 %, respectively.

The pressure coefficient is defined as

$$C_p = \frac{p - p_{ref}}{0.5\rho U_{bulk}^2} \tag{25}$$

where p_{ref} is the pressure at x/L = 0.05 at z/W = 1/2 of lower wall. This coefficient at the outlet section is considered as an indicator of the recovered static pressure and the primary characteristic of a diffuser performance. Conceptually, the pressure coefficient increases with the diffuser aspect ration. However, other practical considerations may affect the design parameters of a diffuser. In particular, the separation of the flow from the walls opening results in a pressure drop due to the dissipative nature of the separated flow. The zero-velocity surface defining the separation boundary acts like a wall that shrinks the outflow area of diffuser. Without careful consideration of the effect of flow separation in a diffuser, higher angle of expansion even adversely reduces the static pressure at the outlet of diffuser. Figure 4 depicts the pressure coefficient along the center-line of the lower wall, i.e. z/W=1/2. The results of Case C show slightly higher-pressure coefficients than the experimental data, while the DNS results are slightly less than

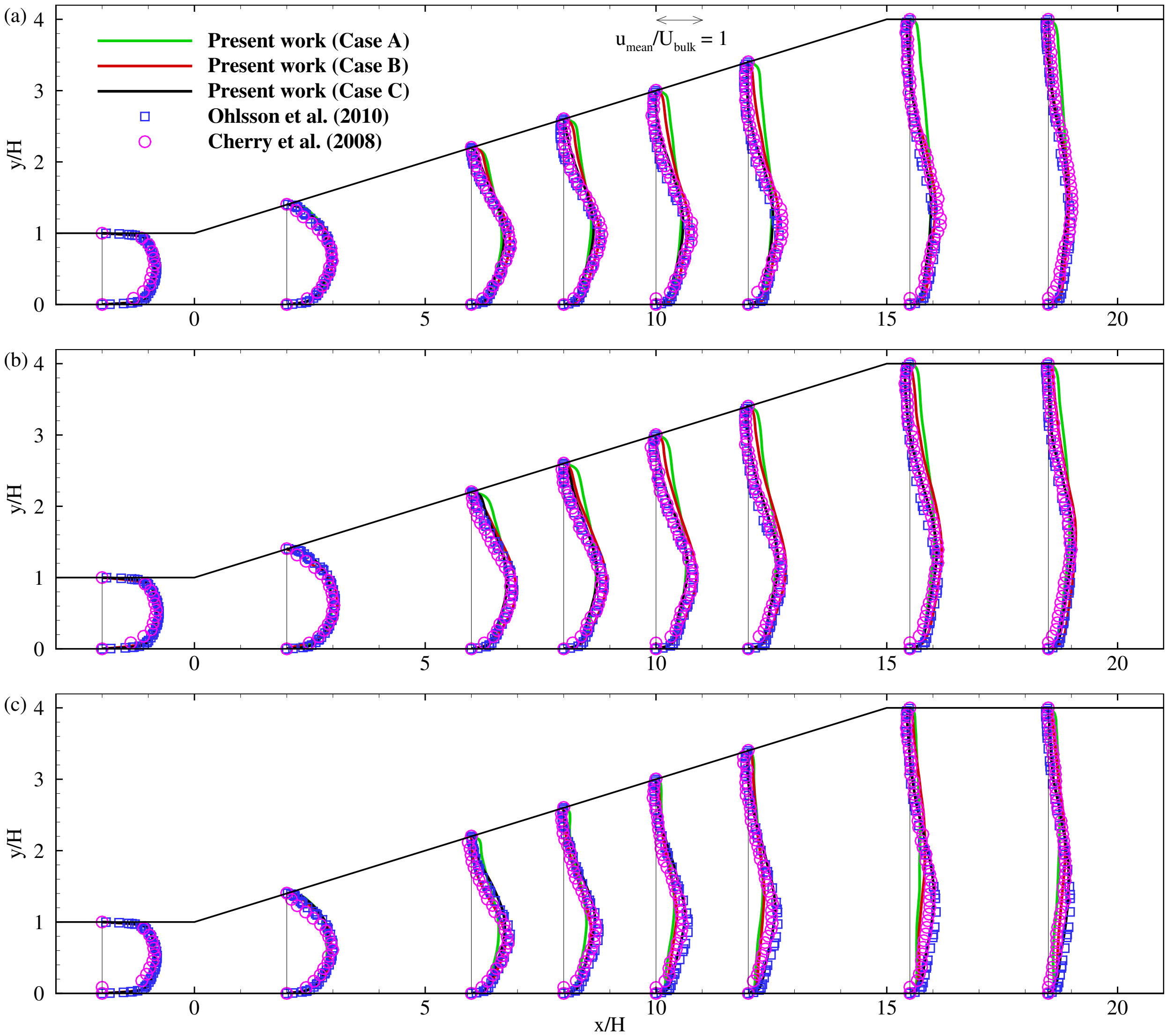

Figure 3: Comparison of present calculated u_{mean}/U_{bulk} profiles with those of Ohlsson et al. [18] DNS results and the measurements of Cherry et al. [16] on x–y planes at z/W = 1/4, 1/2, and 3/4

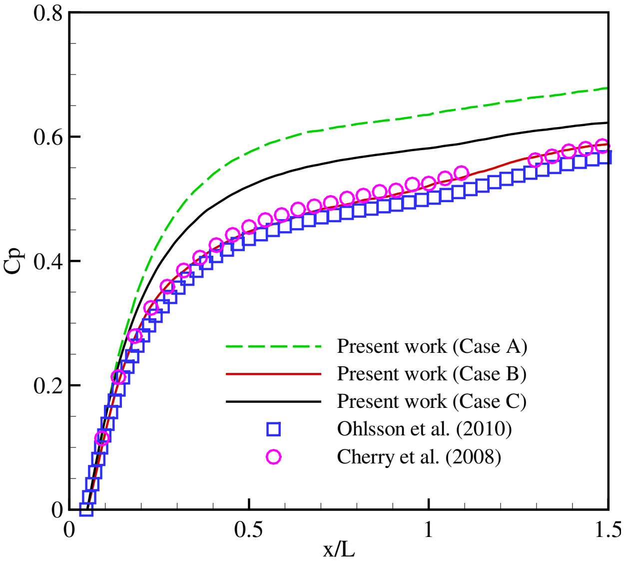

Figure 4: Distribution of pressure coefficient along center-line, i.e. z/W=1/2, on the lower wall (y=0) and comparison with those reported by Ohlsson et al. [18] and Cherry et al. [16]

experimental results. This can be attributed to the fact that the DNS flow computations predicted the separation slightly earlier than that observed in experimental measurements. On the other hand, Case C estimates flow separations more downstream compared to the experimental results. Therefore, the zero-velocity surface calculated by the DNS occupies the outlet section area more than that of Case C. The initial slope of the pressure coefficient variation is similar for DNS, LES, and the experimental results where their velocity profiles matched. Further downstream, the velocity profiles are significantly different for the LES cases, hence, different profiles of the pressure coefficient is observed from the simulations as shown in Fig. 4. Neither the variation nor magnitude of C_p calculated from Case A are not in agreement with those of DNS and experimental results. In Case A, no separation (zero-velocity) surface was predicted by LES calculations, hence, a higher pressure distribution was calculated at the center plane. In other words, there is no mechanism to reduce the effective cross-sectional area within the flow and thus, to limit the non-physical increase of the pressure. In Case B, a flow separation was resolved in partial. Thus, the mean velocity was higher than Case C, where in contrast to Case B, the separation was captured on the upper corners and in the center of the cross-flow plane. As in Case B, the zero-velocity surface is on the upper corners of the side-walls. This pushes the flow towards the center plane. The higher velocity resulted in a lower pressure coefficient, which is in a better agreement with DNS and experimental results in terms of velocity magnitudes. It should be emphasized that the deviation of C_p variation calculated in Case B is potentially attributed to the missing of flow separation in the center of the cross-flow planes. Comparing to the DNS and the experimental results, a higher variation of C_p was calculated for Case C at $x/L \leq 0.6$

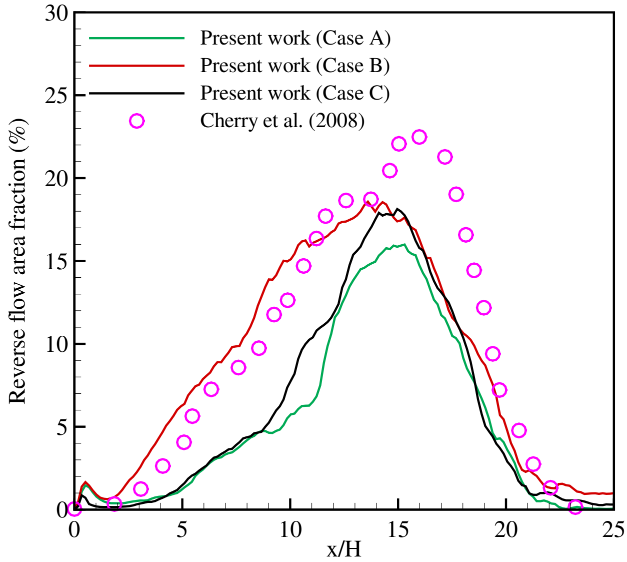

Figure 5: Fraction of reverse flow area along dimensionless streamwise distance from the diffuser inlet and comparison with those reported by Cherry et al. [16]

where a flow separation is predicted. As seen in Fig. 4, beyond the separation point, the slope of C_p profile is similar to what calculated by DNS and experimental results.

Figure 5 demonstrates reverse flow area fraction, which is defined as

$$\text{Reverse flow area fraction}(\%) = \frac{\text{Area of reverse flow}}{\text{Area of the section}} * 100. \tag{26}$$

The pressure coefficient in the diffuser is significantly affected by this ratio. While, the flow pattern calculated in Case B deviates from the measurement, the estimated pressure magnitude is the closest one to the experimental results along the first half of the diffuser passage. Moreover, this figure indicates that although the calculated pressure coefficient in Case C follows a similar trend to the experimental results, its magnitudes differs slightly from the measurements.

Figure 6 shows the profiles of the turbulence intensity and ratio of the resolved to total turbulence energy for Cases A, B, and C at the center plane, i.e. z/W=1/2. The turbulence intensity profiles are compared with those of DNS results and experimental data. In Fig. 6(a), the variation of turbulence intensity is not in agreement with the reference results for Cases A and B, as in these cases where no flow separation was resolved at the center plane. On the other hand, the results obtained for Case C show a similar trend to those of the experimental and DNS profiles with a small difference in magnitude. The origin of this difference is attributed to fact that the present LES flow computations are carried out on a coarser grid compared to the DNS, especially, along the streamwise direction. One can observe in Fig. 6(a) that the intensity in the separated region is less than other regions. This is due to the low energy of resolved eddies and the small reverse flow velocity in this region. Figure 6(b) shows the ratio of resolved to total TKE at the center plane.

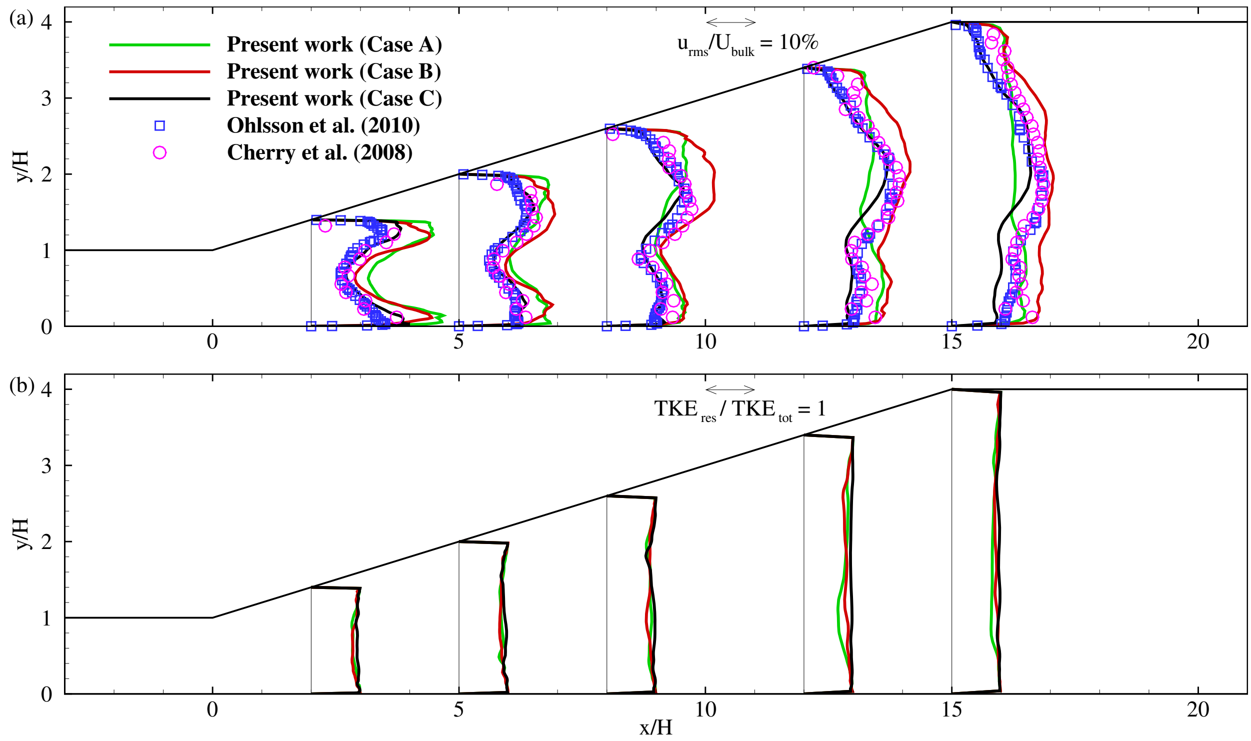

Figure 6: The profiles of (a) the turbulence intensity and (b) the ratio of the resolved to total TKE at z/W=1/2

The resolved TKE is

$$\mathrm{TKE_{res}} = \frac{1}{2}(\overline{u_x'^2} + \overline{u_y'^2} + \overline{u_z'^2}) \tag{27}$$

where $\overline{u_i'^2}$ is the averaged square of resolved velocity fluctuations, and the total TKE is

$$\mathrm{TKE_{tot}} = \mathrm{TKE_{res}} + \mathrm{TKE_{SGS}}. \tag{28}$$

The ratio of resolved to total TKE is an indicator of the performance of LES simulations. As it can be seen in Fig. 6(b), this ratio is closer to unity for Case C compared to Cases A and B. This confirms that more TKE was resolved in Case C.

The evaluation of the present LES computations is progressed by examining the power spectral density (PSD) at selected computational points (probes) within the flow domain. The probes are located in the area where, as shown in Fig. 6(b), cases have the highest difference of the ratio of resolved to total TKE. For this purpose, the temporal variation of resolved TKE is expressed in terms of the frequency and presented in Fig. 7. In this figure, the PSD diagram is plotted in a logarithmic scale for two probes located at (x,y,z)=(6H,H/2,W/2) and (12H,H/2,W/2). The results show that the overall slope of PSD in Case B and Case C are closer to the expected value of $-5/3$ than Case A which states that the energy transfer from large-scale (energy carrying) to small-scale (dissipating TKE) eddies was captured better in Case B and Case C at probe points. The area below the diagram at both points for case B is larger than case C,

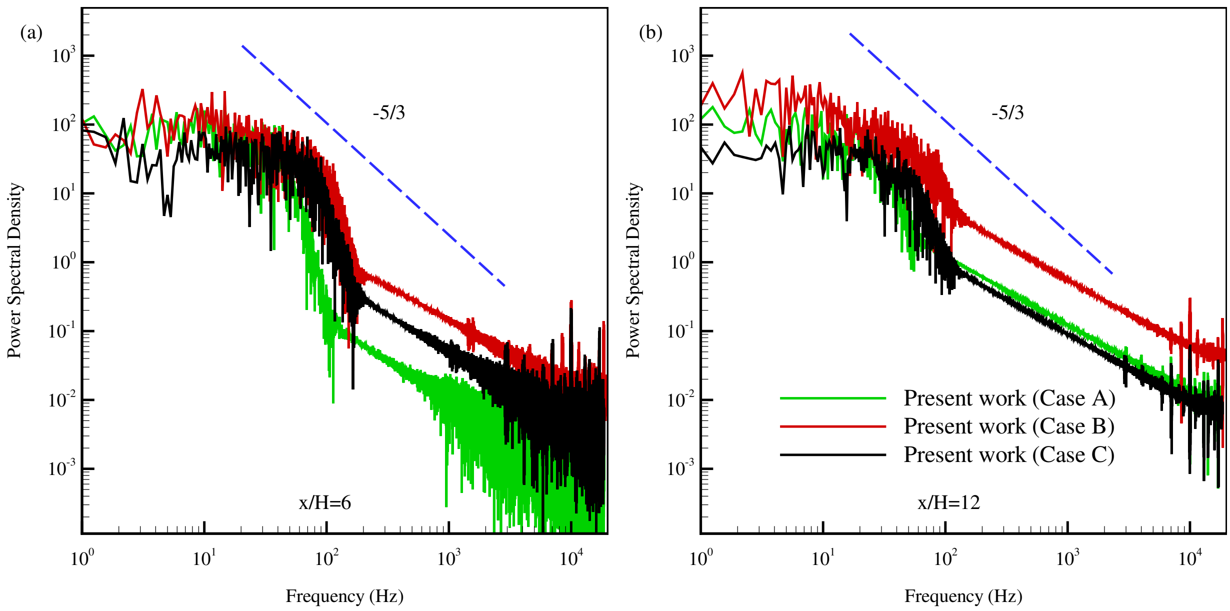

Figure 7: PSD diagrams for two selected probes located at x/H=6 and 12 on the plane y/H=z/W=1/2.

indicating the larger calculated turbulence kinetic energy at these two points. Figure 6(a) also confirms that the turbulence intensity in case B is higher than case C and the experimental results and DNS in regions close to the location of the probes. The ratio of the area under the diagram before changing the concavity to the total area of the under diagram in the PSD diagram for case C is greater than case B at probe points, which is confirmed by Fig. 6(b). This ratio represents the resolved turbulence kinetic energy to the total turbulence kinetic energy. From the PSD plots for Case C in Fig. 7, it is concluded that the eddies with frequency lower than and above 200 Hz were resolved and modelled, respectively. Given the accuracy of the present results, this confirms that the employed computational temporal and spatial grids provide an acceptable cut-off frequency for the present LES of the studied problem.

Figure 8 shows the PSD diagram calculated in terms of velocity fluctuations in the streamwise direction. As seen, as the computational grid is refined in the streamwise direction, the slope of PSD diagram approaches to the expected magnitude. Since the streamwise resolution of the grids is the same for both Case B and C, their slope is similar in Fig. 8 at x/H=6 and 12. At x/H=6, the concavity of the graph in Case B has changed at a lower frequency than in Case C. This shows the effect of grid resolution in the normal and spanwise direction on the accuracy of turbulence characteristics in the streamwise direction. These effects are less at x/H=12 because as the flow establishes forward in the diffuser, the velocity gradient at the walls decreases and the dimensionless parameters Δy^+ and Δz^+ are in an appropriate range at probes.

To provide another view point for LES flow calculations at one of the most intense flow recirculation zones, a probe was located at x/H=14.5, z/W=1/2, and y/H=3.3. Here, the results of Case C showed an

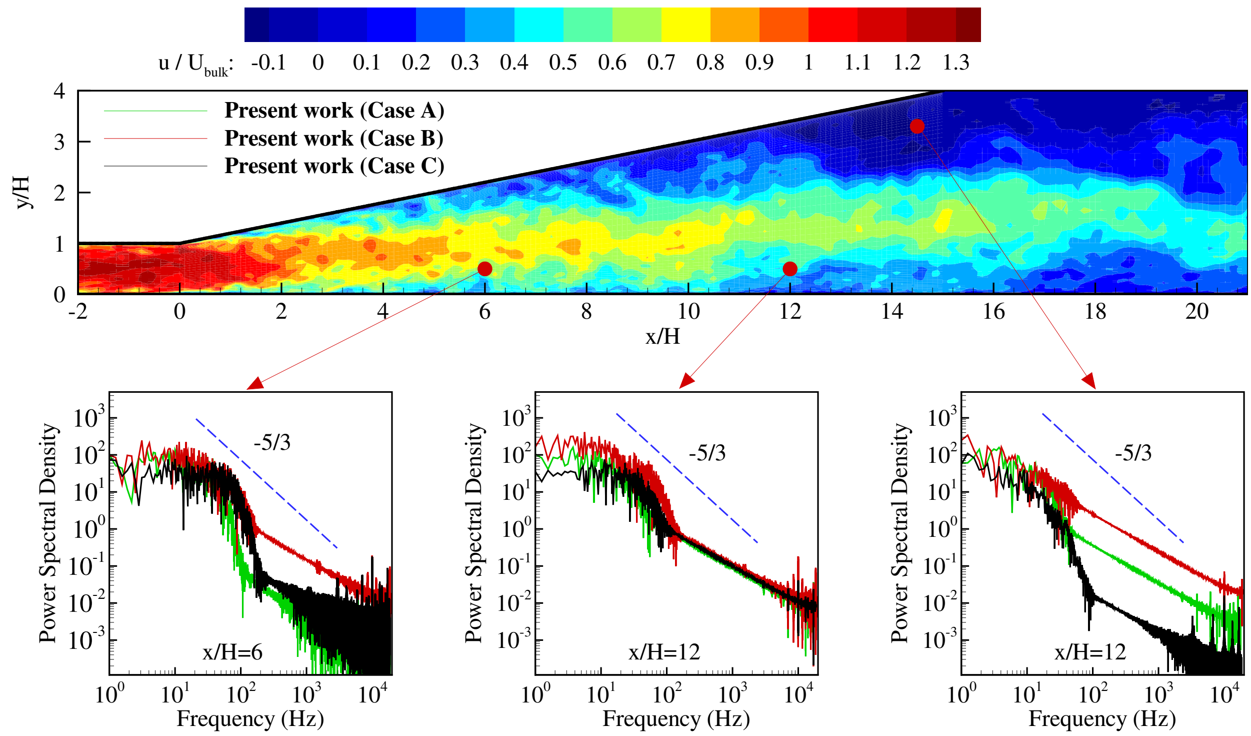

Figure 8: Contours of calculated u/U_{bulk} of Case C at z/W=1/2 and associated PSD diagrams in streamwise direction for three selected probes at x/H=6, 12 and 14.5.

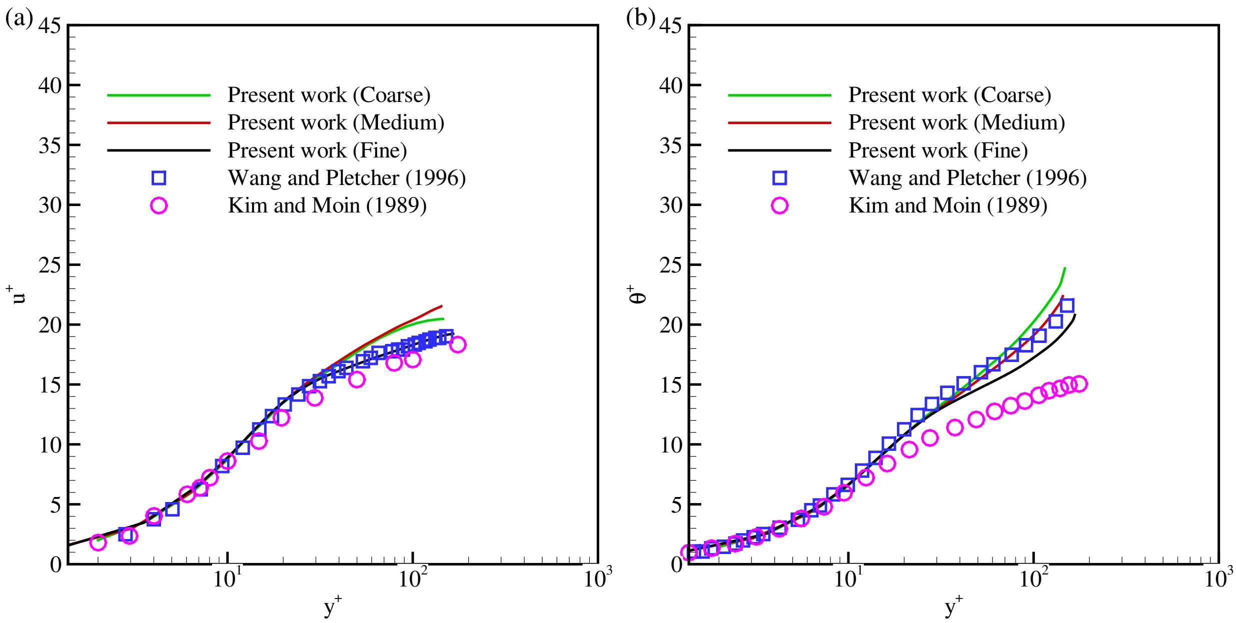

Figure 9: Flow and heat transfer computations in a three-dimensional channel; (a) fully-developed velocity profile (b) non-dimensional temperature.

area under the PSD diagram smaller than those of for Case A and B. In other words, the total TKE is significantly lower than two other cases at this location of the diffuser. This difference is attributed to that Case C predicted the separation at x/H=14.5 and z/W=1/2 while two other cases did not.

The computation of air flow and heat transfer through a three-dimensional channel was used as a standard test case to validate the present extended temperature solver. Three computational girds were used to perform validation and their details are given in Table 2. The temperature of the top, and bottom walls were set to 303K and 297K, respectively. A fully developed velocity profile at temperature of 300K was obtained by performing cyclic flow calculation and imposed at the inlet section. In Fig. 9, the dimensionless velocity and temperature profiles of the validation case are compared with those of DNS results reported by Kim et al. [46] and Kim and Moin [33], respectively. Also, the results of LES calculations provided by Wang and Pletcher [47] are included in Fig. 9. The dimensionless temperature is defined as $\theta^+ = T - T_{wall}/\theta^*$ where θ^* is the friction temperature and expressed by

$$\theta^* = \frac{\alpha}{u^*} \left.\frac{\partial T}{\partial y}\right|_{wall} \tag{29}$$

In this figure, the obtained fully developed dimensionless turbulent velocity and temperature profiles are in good agreement with the results presented by Kim et al. [46] and Kim and Moin [33], respectively.

Another validation has been undertaken to assess suitability of the extended solver in turbulence separated flow regimes. For this purpose, a standard backward-facing step with the Reynolds number of 5540 (based on the step height and upstream centerline velocity) has been considered. The physical parameters

Table 2: Specifications of computational grids employed to solve temperature field within channel.

Case	n_{x}	n_{y}	n_{z}
Coarse	50	32	32
Medium	50	64	64
Fine	100	64	64

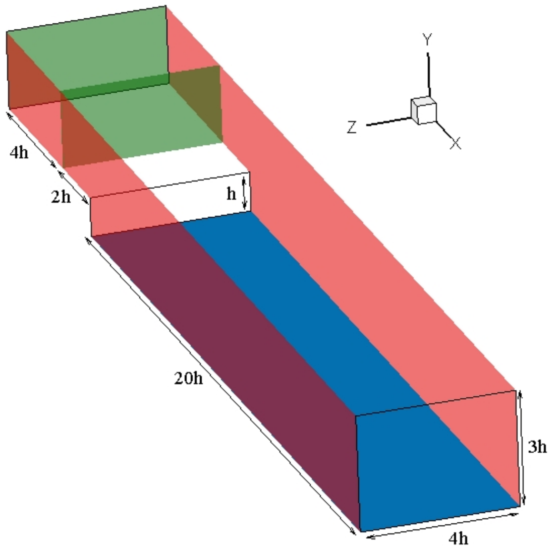

Figure 10: Backward-facing step geometry; the inlet and the mapped planes are specified by green, cyclic lateral walls are specified by red, and heated lower wall is specified by blue.

for this simulation are $\mathrm{U_c} = 2.063\,\mathrm{m/s}$, $\mathrm{U_{bulk}} = 1.79\,\mathrm{m/s}$, $\mathrm{T_{in}} = 293\,\mathrm{K}$, $\nu = 1.527\mathrm{e}^{-5}\,\mathrm{m^2/s}$, and $\mathrm{Pr} = 0.71$. The geometry of the step has been shown in Fig. 10, where the height of step is h=0.041 m. A total grid number of 244512 have been used for the calculation. The grid distribution upstream of the step was $\mathrm{n_x} = 40$, $\mathrm{n_y} = 31$, and $\mathrm{n_z} = 48$ and downstream of step was $\mathrm{n_x} = 82$, $\mathrm{n_y} = 47$, and $\mathrm{n_z} = 48$. Mapped field condition has been set in the inlet boundary to feed a turbulence fully developed flow into the domain. The cyclic boundary condition has been set on lateral walls. The non-slip and adiabatic boundary condition has been set on the upper wall and the non-slip and constant heat flux of $1000\,\mathrm{W/m^2}$ has been set on the lower wall.

LES calculations have been performed with $\mathrm{Pr_t} = 0.85$ and maximum Courant number of 1. Figure 11(a) shows the dimensionless velocity profiles which were compared with measurements of Kasagi and Matsunaga [48] and the LES calculations of Avancha and Pletcher [35]. Present results have shown a better agreement with experimental velocity profiles in comparison with LES results of Avancha and Pletcher [35] and predicted a larger recirculation length in agreement with the experimental results of Kasagi and Matsunaga [48]. The length of main recirculation zone for present work, DNS results [34], and prediction of

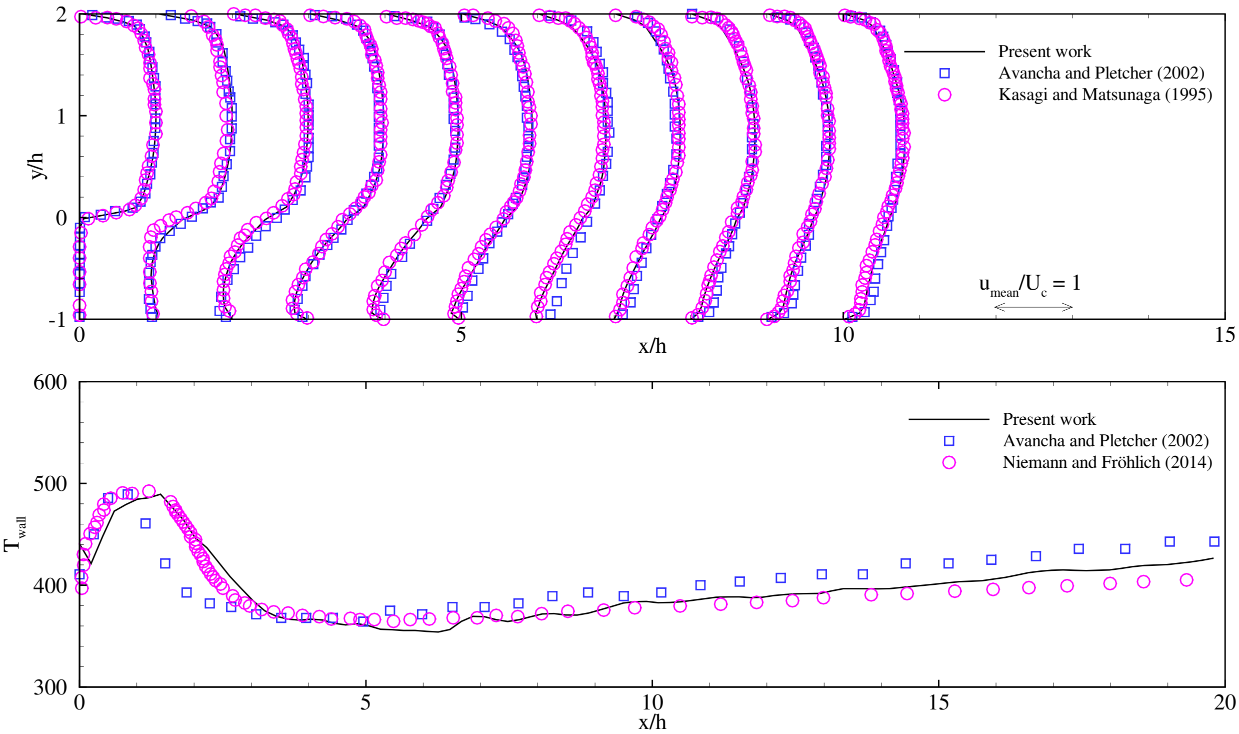

Figure 11: Backward-facing step results; The profiles of (a) dimensionless velocity and (b) temperature on the lower wall

Avancha and Pletcher [35] are 5.25 x/h, 5.1 x/h, and 4.16 x/h, respectively. Also, the re-attachment point has been predicted in present work at x/h=7.06 while x/h=6.51 reported in the experiment and the LES result of Avancha and Pletcher [35] predicted at x/h=6.1. The profile of temperature on the lower wall has been compared to the DNS result of Niemann and Fröhlich [34] and LES result of Avancha and Pletcher [35] in Fig. 11(b). The overall trend of temperature profile is consistent with other numerical results. A minor local minimum temperature can be seen downstream of the step due to the prediction of higher velocity in the corner of step and lower wall compared to the experimental results. As a result of better recirculation length prediction, the maximum wall temperature has been shifted downstream in comparison with the LES result of Avancha and Pletcher [35] and in agreement with the DNS result of Niemann and Fröhlich [34]. Because of assuming constant density and Prandtl number, the present and the DNS results have shown smaller increase in temperature after the reattachment in comparison with the LES of Avancha and Pletcher [35], whereas variation of density and Prandtl number are considered.

The contours of the streamwise velocity on different cross-flow planes are given in Fig. 12 for Case C. The velocity contours are compared with those of DNS simulation and the experimental data. In the present results, the separation started from the top corner at the expanding sidewalls and extended to the diffuser center. This is in agreement with the experimental data and the DNS results. Moreover, the separation started from both upper corners which is in agreement with the measurements performed by Reneau et al.

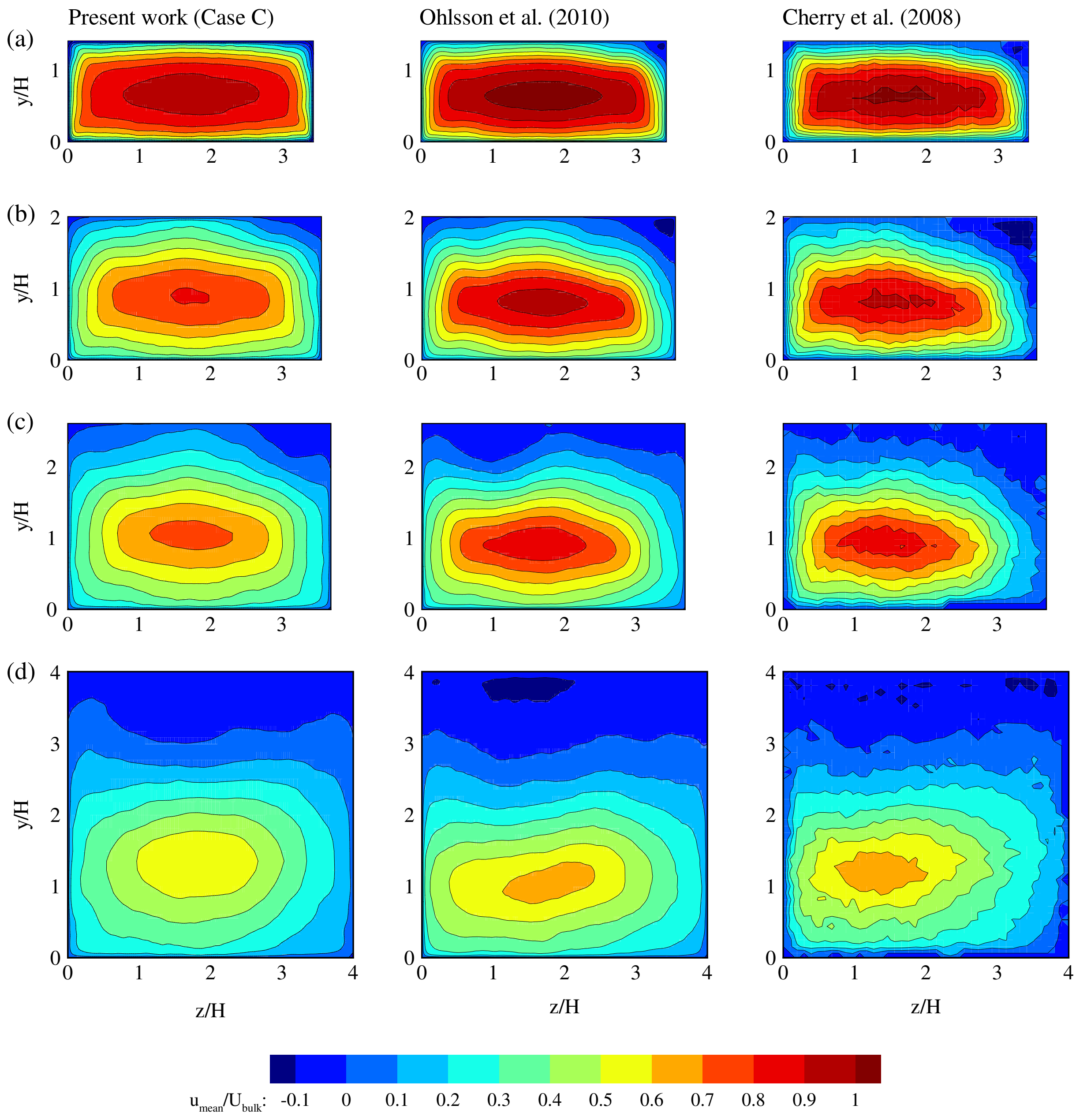

Figure 12: Crossflow planes of streamwise mean velocity at (a) $x/H = 2$, (b) x/H=5, (c) x/H=8 and (d) x/H=15 of the diffuser which located at zone III. Here, left, middle, and right columns are the present LES result (Case C), Ohlsson et al. [18] DNS result, and Cherry et al. [16] measurements, respectively.

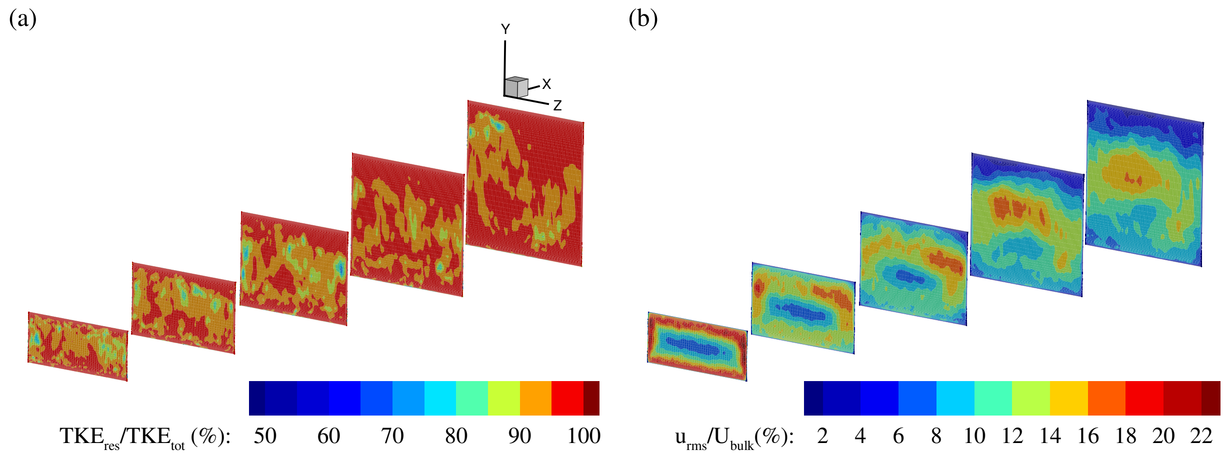

Figure 13: Contours of the (a) ratio of the resolved to total TKE and (b) turbulence intensity at cross-flow planes with x/H=2, 5, 8, 12, and 15.

[17] who studied the separation regions in diffusers. In this figure, a more significant separation is also predicted on the top right, where the two diverging walls meet, in comparison with the top left corner. Ohlsson et al. [18] pointed out that there is a bump shape of the velocity contours due to the presence of a secondary flow structure in the cross-flow plane at x/H=8. However, in the current LES result, the bump shape is predicted on the cross-flow plane at x/H=15. In comparison to the DNS results, the flow separation obtained from the present numerical experiments is located at a section with higher x/H in downstream.

Figure 13 shows the contours of the ratio of the resolved to total turbulence energy and turbulence intensity at cross-flow planes with x/H=2, 5, 8, 12, and 15. The LES results can be categorized into classes in terms of the fraction of the resolved TKE. In near-wall resolved class, the spatial and temporal filters are adequately small for resolving almost 80% of TKE in the entire flow field. On the other hand, in near-wall modelled class, the time filter and grid resolution are set to resolve almost the same fraction of the off-wall TKE. In a very large eddy simulation technique, less than 80% of TKE is resolved employing a coarse time-step and grid resolution [49]. The results of resolved TKE ratio of Fig. 13(a) demonstrate that more than 80% of the TKE has been resolved on Case C for the most of the flow domain, therefore the simulations are placed in the LES near-wall resolved class. At a crossflow plane, there are a few spots where less than 80% of the TKE has been resolved. Back to Fig. 3, the velocity profiles show that the regions with more than 80% homogeneously resolved TKE are in a better agreement with the DNS results and measurements. However, the velocity profiles deviate from referenced data in regions with a scattered resolved TKE where its magnitude is either above 90% or below 70%.

As expected, the flow experiences a decrease in turbulence intensity beyond the separation surface and an increase after the re-attachment point. This has been confirmed by the results of Fig. 13(b) at the

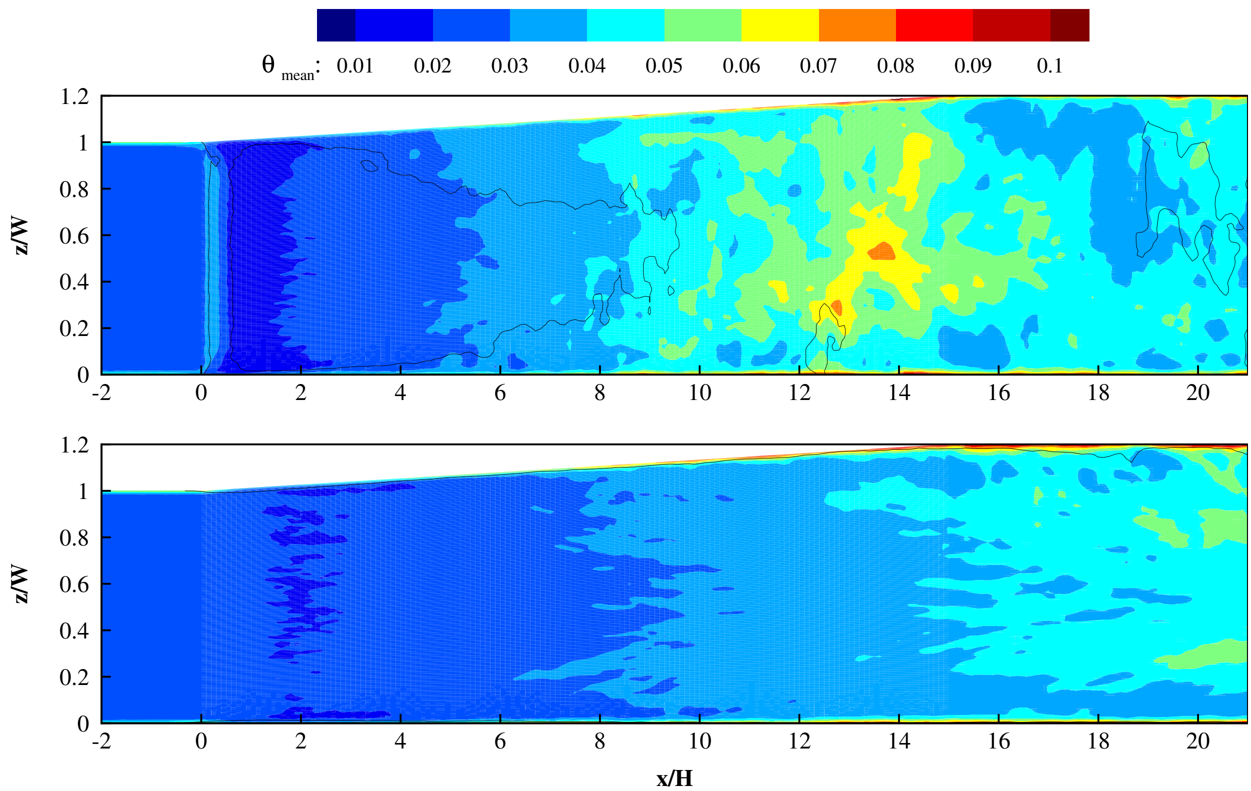

Figure 14: Contour of dimensionless mean temperature of the diffuser walls: (a) upper wall and (b) lower wall. Solid black line depicts the locations where a zero value is calculated for the normal velocity gradient.

crossflow planes. The lowest value of the turbulence intensity is achieved in the separated flow region. The numerical experiments exhibit that the turbulence intensity is higher on the expanded wall compared to the fixed wall. This is in agreement with the experimental observations reported by Cherry et al. [16].

The thermal calculations were performed for Case C using the extended temperature solver. The properties considered for the fluid, namely the Prandtl number and the thermal diffusivity, are those of water in the present numerical experiments. Figure 14 shows the contours of dimensionless mean temperature (θ_{mean}) on the upper and lower walls of the diffuser. The numerical results show that the temperature on the upper wall is affected by the zero velocity gradient lines. The regions where the flow is separated have been subjected to higher wall temperatures than the other areas with attached flow. The convective heat transfer coefficient decreased significantly near the solid wall adjacent to the separated flow. On the lower wall, an increment in the temperature is observed in the separation region at left lower corner. Considering the flow Reynolds and water Prandtl numbers, the effects of the temperature rise at the upper wall are small on the lower wall temperate distribution.

To investigate the heat transfer mechanisms in the separated flow region, the iso-surfaces of i) zero

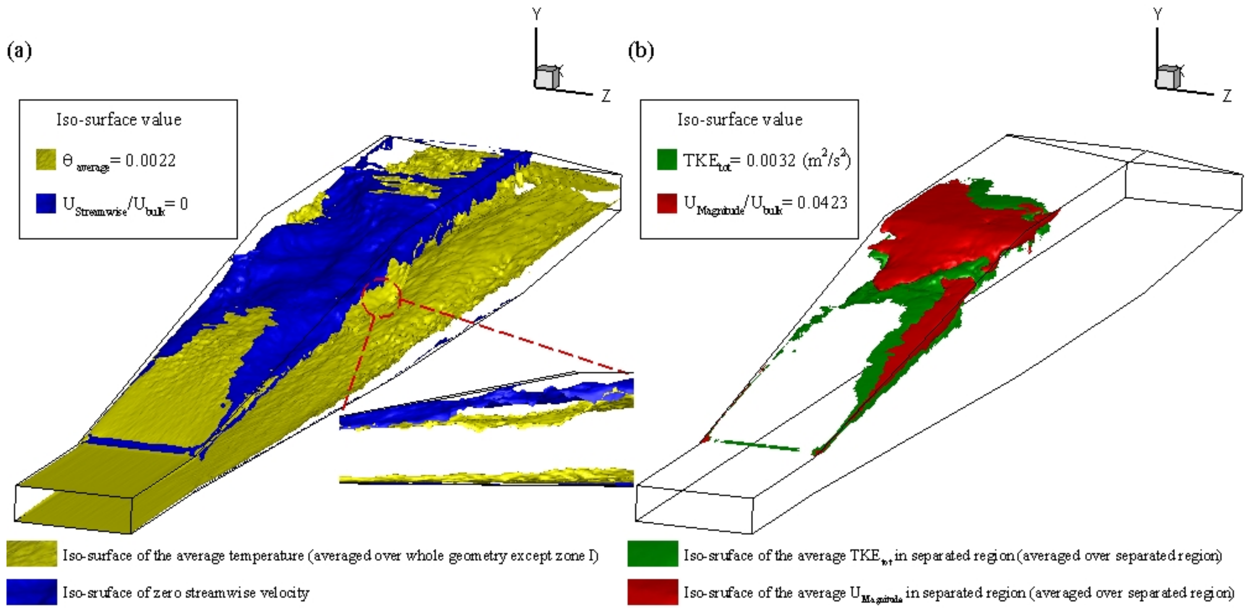

Figure 15: iso-surfaces of (a) the average dimensionless temperature of domain (gold) and zero streamwise velocity (blue) (b) the average total TKE (green) and the average velocity magnitude of separated zone (red; the dashed red lines show a view from the z direction for the specified area

streamwise velocity, ii) the average temperature of the domain, iii) the average total TKE at the separated zone, and iv) the average velocity magnitude of the separated zone are shown in Fig. 15. The topology of iso-surface of zero streamwise velocity reveals that the flow separation begins from the corners, and it intensifies along the lateral expanded wall. The flow separations establish from the corners along the upper wall and meet around x/H=9.5. The flow re-attachment starts around x/H=19 and ends at top corners around x/H=21. As can be seen in Fig. 15(a), as the blue area started to develop, the gold surface distanced from the upper wall, i.e. the size of region with higher temperature than average is increased. Since the heat flux of the upper wall is constant, the growth in the high temperature region implies that the region with poor heat transfer coefficient is enlarged due to the flow separation. Likewise, the low temperature can be attributed to high local heat transfer. There is a region near the fixed wall, where the blue and gold surfaces meet, which contains separated flow with temperature lower than the average of the domain. As seen in Fig. 15(b), most of the regions, with higher momentum and turbulence intensity than average of the separated zone, are located near the fixed wall. This can explain presence of a high local heat transfer region near the fixed wall where the blue and gold surfaces intersect.

For better understanding of characteristics of the flow around local hot spots, which can be seen in Fig. 14, the flow and temperature fields in vicinity of the spot with the highest temperature have been considered. Figure 16 shows contours of velocity magnitude, total TKE and dimensionless mean temperature on the

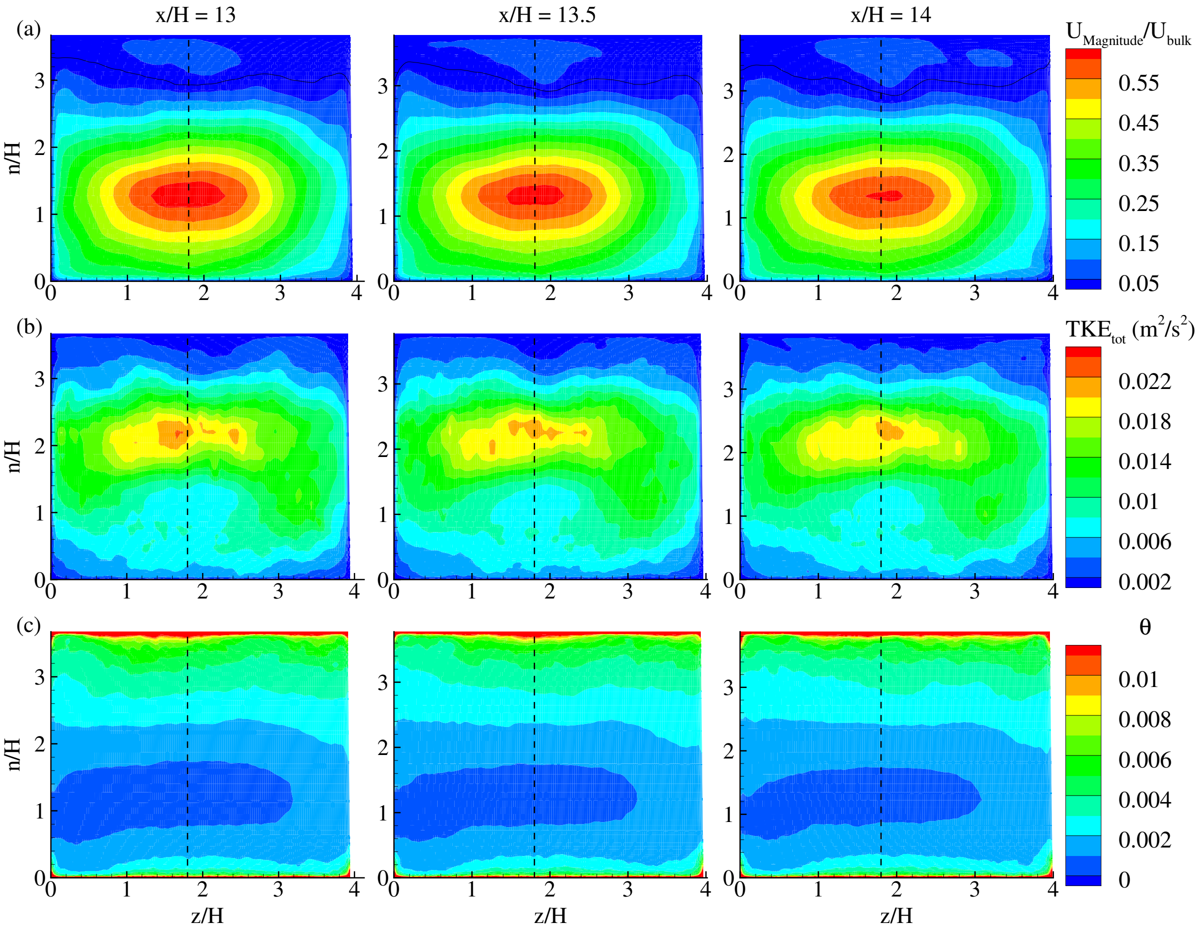

Figure 16: Contour of (a) velocity magnitude, (b) total TKE and (c) dimensionless mean temperature at x/H=13, 13.5, and 14. Solid black lines depict the locations where a zero streamwise velocity is obtained. Dashed black lines indicate location of the selected hot spot.

planes normal to the upper wall at x/H=13, 13.5, 14. The velocity magnitude and total TKE are considered as the main mechanism and indicator of the turbulent power incorporating the heat transfer in a turbulent separated flow. In Fig. 16(a), the magnitude of velocity within the regions around the selected hot spots does not show an effective difference. On the other hand, the thickness of low TKE layer in the hot zone is higher than the surrounding areas (see Fig. 16(b)). This plays the role of a thick insulator and reduces the heat transfer coefficient in the region above the hottest spots on the upper wall. This behaviour of low TKE layer occurs due to lack of downwash effect as discussed by Keating et al. [50]. In this region, eddies hardly bring cold fluid from the region above the shear layer towards the wall because of low wall shear stress fluctuations.

Figure 17 shows the time-averaged dimensionless velocity gradient normal to the upper and lower walls at z/W=1/4, 1/2, and 3/4. In this figure, locations on the upper wall with either a zero or negative velocity

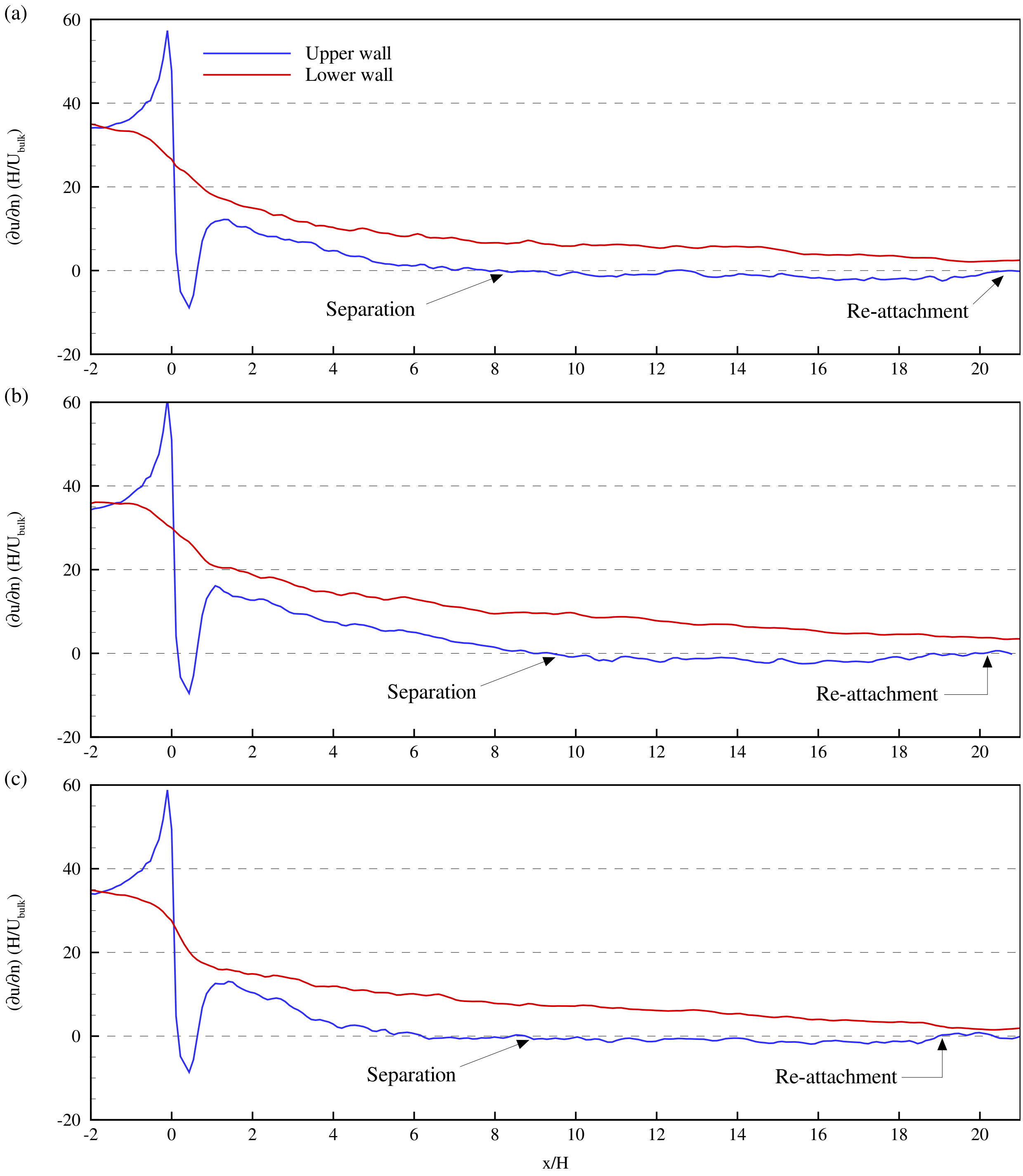

Figure 17: Time-averaged dimensionless velocity gradient normal to the upper and lower walls at (a) z/W=1/4, (b) 1/2, and (c) 3/4.

gradient corresponds to the regions where the flow is separated. At selected z/W coordinates, the main flow separation is predicted on the upper wall at x/H=8.2, 9.5, and 8.8 and and corresponding re-attachments at x/H=21, 20.5, and 19. The results show local separations and re-attachments upstream of the main flow separation points. It is emphasized that the velocity gradient calculated for the flow adjacent to the upper wall is influenced by the flow separation on the sidewall. Therefore, the velocity gradient normal to the wall is an acceptable indicator for investigating the heat transfer characteristics of the upper wall.

Figure 18 shows the variation of time-averaged dimensionless wall temperature at selected z/H coordinates. There is a significant increment in the wall temperature in the separation region. As mentioned before, this indicates a decrease in the convective heat transfer coefficient resulting from the low velocity and kinetic energy transfer in the separated flow within the boundary layer. In another view, the regions with low velocity and TKE play the role of a thermal isolating layer and consequently, reduce the heat transfer from the wall. In the separation area, the temperature reaches its highest level and then decreases toward the re-attachment point.

Figure 19 shows the variation of Nusselt number of the upper wall at selected z/H coordinates. The Nusselt number distribution shows a local minimum beyond the separation point. It increase beyond the re-attachment point indicating more heat transfer flux from the wall. As is seen, the numerical results indicate that an increase in the turbulence intensity results in an enhancement in the heat transfer between wall and fluid flow. The flow experienced local high TKE slightly before the re-attachment zones, which resulted in the local high Nusselt number.

The Reynolds analogy states that skin friction coefficient ($C_f = \tau_w/\frac{1}{2}\rho_\infty U_\infty^2$) and Stanton number ($St = Nu/Re_\infty Pr_\infty$) are directly related and behave in the same way. Given that in the current problem the Reynolds and Prandtl numbers are constant, the Reynolds analogy implies that the Nuesselt number varies proportionally with skin friction coefficient. As is seen in Fig. 17 and 19, this statement is established for the lower wall in all three planes and both diagrams show a downward trend. However, on the upper wall and in the separation zone, the variation of skin friction coefficient is not similar to the variation of Nusselt number. For instance, a minimum for local Nusselt number is calculated about x/H=14 at all three planes in Fig. 19. However, a different variation is predicted for the skin friction coefficient. Moreover, in contrast to the skin friction coefficient, a step increase is calculated for the Nusselt number where an increase of TKE is predicted in the area prior to the reattachment zone. This implies that the Reynolds analogy does not hold in the separation regions, which is in agreement with the findings of Vogel and Eaton [51], Avancha and Pletcher [35] and Keating et al. [50].

Considering the above discussions, since the Reynolds analogy is no longer valid in the area bounded by the zero normal velocity gradient lines, there is no direct relationship between the local high temperature zone and the zero normal velocity gradient. It can be realised that a low local heat transfer coefficient is calculated at the most of the wall surface adjacent to the separation zone due to the low momentum

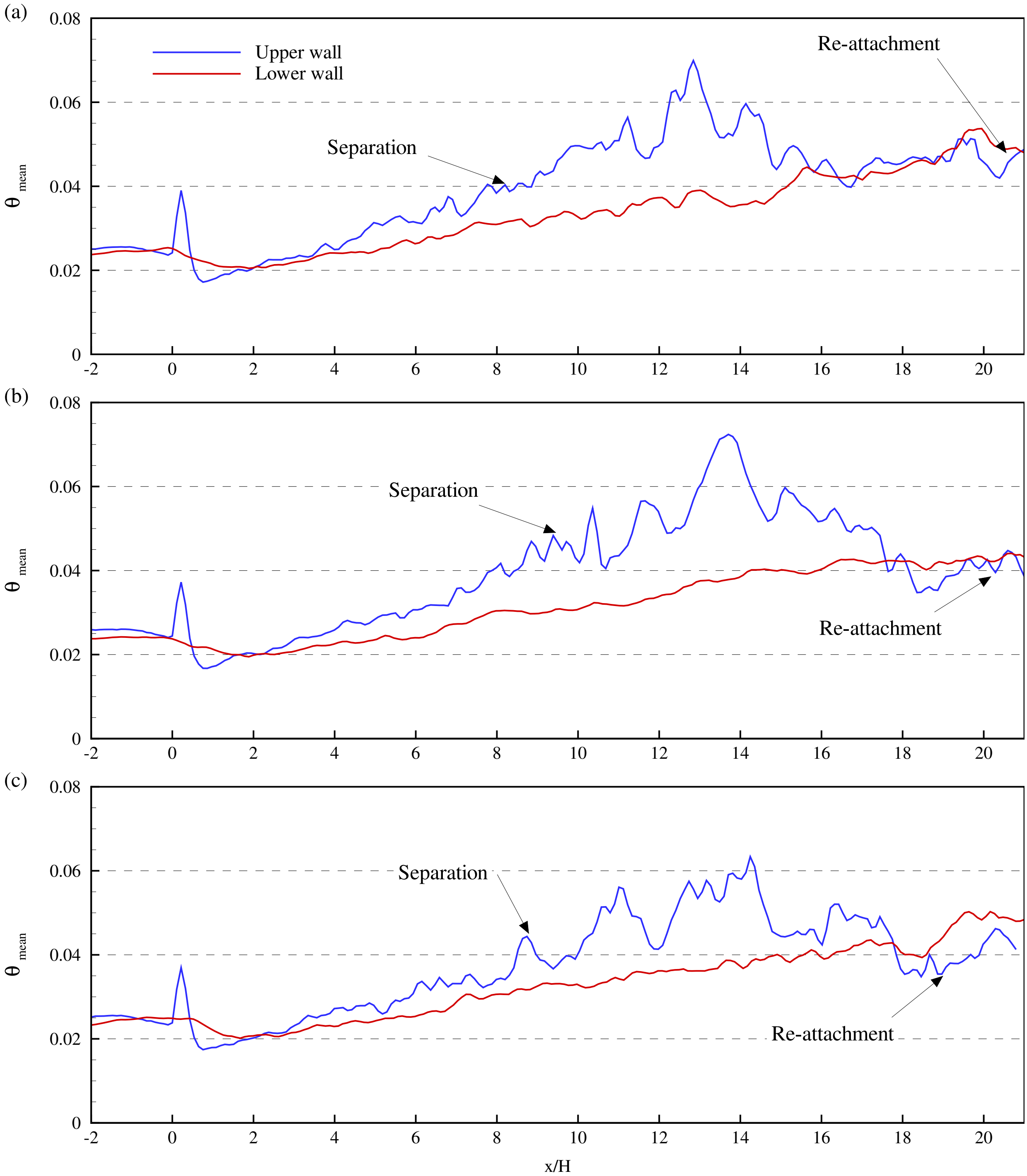

Figure 18: Time-averaged dimensionless temperature along upper and lower walls at (a) z/W=1/4, (b) 1/2, and (c) 3/4.

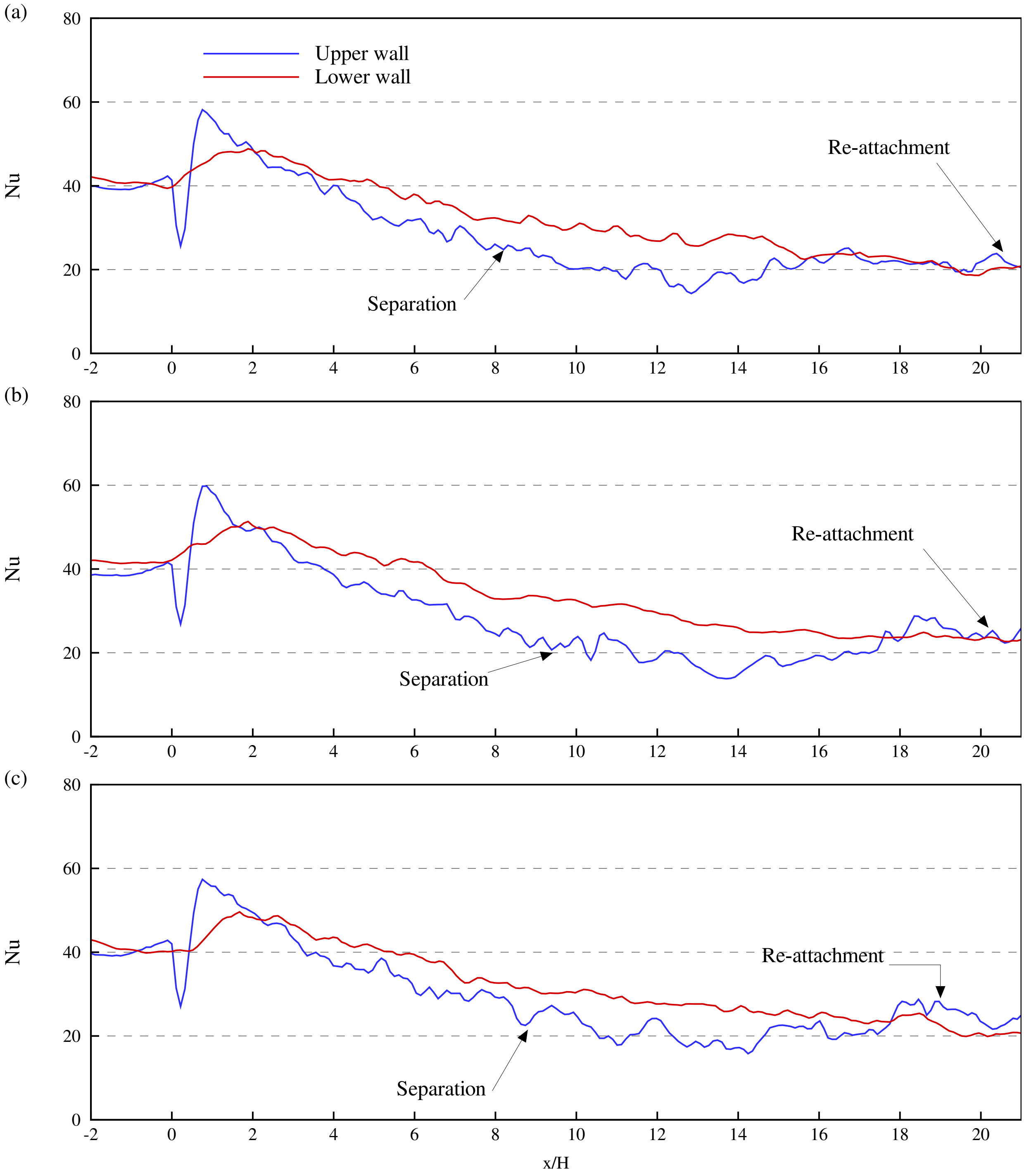

Figure 19: a) Nusselt number on wall at z/W=1/4 on upper and lower wall; b) Nusselt number on wall at z/W=1/2 on upper and lower wall; c) Nusselt number on wall at z/W=3/4 on upper and lower wall

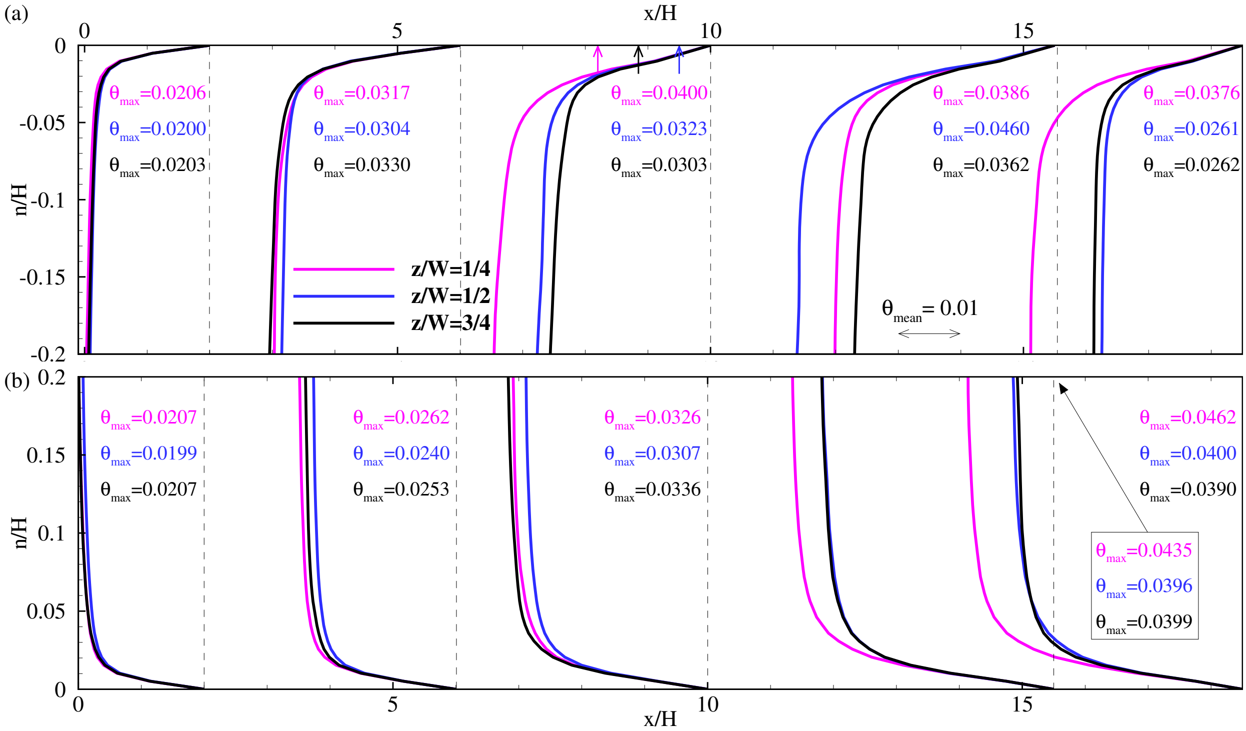

Figure 20: Dimensionless mean temperature profiles normal to the (a) upper and (b) lower walls at z/W = 1/4, 1/2, and 3/4.

and turbulence intensity in the outer layers. Therefore, in addition to the effect of zero normal velocity gradient, low momentum and turbulence kinetic energy result in building a local low Nusselt number and consequently, a local high temperature zone.

Figure 20 shows the dimensionless mean temperature profiles normal to the upper and lower walls in the thermal boundary layer at selected z/H coordinates and x/H = 2, 6, 10, 15.5, and 18.5. Also, n indicates direction normal to the wall. In Fig. 20(a), the arrows indicate the separation points at the upper wall. A temperature increase is predicted beyond the separation point on upper wall. The bulk flow and upper wall separation had some minor effects on the lower wall temperature profile. Generally, the lower wall and its adjacent flow temperature increases monotonically as the flow advances along the diffuser. However, the rate of increase is not the same at different spanwise locations, see Fig. 20(b). Flow separation starts from the top corners and therefore, its effects are more obvious at the flow sheet with z/W=1/4 then the ones with z/W=1/2 and 3/4. Furthermore, on plane z/W=1/4, the flow reattachment length is higher than the other planes (see Fig. 17). Therefore, a lower heat transfer coefficient is calculated in this plane which results in a higher temperature at the top wall. The increase of the temperature on this plane has affected the temperature distribution of the lower wall at z/H=1/4. This can be observed in Fig. 20(b) where the temperature at z/W=1/4 has the highest increase compared to the other two planes. As seen in Fig. 12, the largest separated area and consequently, a lower heat transfer is calculated for z/W=1/2 and x/H=15.

Table 3: Comparison of the computational cost and parallelisation performance of Case A, Case B, Case C and Case C with thermal calculations according to number of iterations, the computation time, and the number of cores.

Parameters	Case A	Case B	Case C	Case C*
ANI of the momentum equation	7.323	7.913	8.617	8.630
ANI of the pressure equation	233.6	169.0	54.97	53.88
ANI of the temperature equation	—	—	—	2.000
Total ANI	240.9	176.9	63.59	64.52
Averaged execution time (sec)	4.469	3.937	1.965	1.950
Averaged clock time (sec)	4.493	3.972	2.006	1.996
Relative NCPL (%)	0.534	0.888	2.066	2.357
Number of time steps ($\times 10^3$)	60.44	63.57	57.96	58.41
Computational cells per core ($\times 10^3$)	24.48	22.91	36.23	36.23

* Flow and thermal calculations.

Considering a constant heat flux boundary condition at the wall, a temperature increase is achieved shown in Fig. 20(a) at x/H=15.5. The temperature difference between the planes also depends on the difference in flow intensity and the size of the separation area on that plane. On plane z/W=3/4, as shown in Fig. 13, the flow turbulence intensity is higher than the other two planes, resulting in more heat transfer in this plane. This larger heat transfer causes the temperature on this plane to be lower compared to the other two planes, z/W =1/4 and 1/2.

Computational cost and performance

The performance of the parallelisation of the computations has been studied by looking at the computational cost, namely the number of computation cores and the execution and communication times. A high-performance computing cluster with 16 nodes each consists of two six-core Intel Xeon E5-2620 2.0 GHz CPUs, and 64 GB RAM has been employed for numerical simulation except for Case A, where the simulations were performed over 8 nodes. The computations data are denoted in Table 3 for 4 flow-through time (τ) of the simulations where the averaging was performed. For the purpose of comparison, the number of iterations are averaged over the number of time steps denoted by averaged number of iterations (ANI). The execution time is the exact time of CPUs execution and the clock time is defined as the total CPUs time. The nodes communication power lost (NCPL) is defined as the difference between the clock time and execution time, representing the time the data is transmitted between nodes. Relative NCPL is defined as the ratio of the NCPL to the execution time. Since the time step was not constant and instead controlled by a maximum Courant number, the number of time steps for Case C with thermal calculations is greater than the number of time steps for the same case without thermal calculations. Adding the temperature equation did not affect the execution time significantly as the velocity field was calculated from the flow equations. However, adding the temperature equation affected the data transfer time and increased waste power since it introduced additional data. Reduction in of pressure iterations for Case C resulted in a significant saving in the average clock time in comparison with Case A and Case B. this was due to better mesh quality for Case C. As it can be concluded from Table 3, the convergence speed increased by increasing the grid number. Obviously, there should be a trade-off between the computation cost for a large grid and the convergence speed. Case A has the lowest relative NCPL, while Case C experienced the highest. The increase in NCPL occurs either due to a decrease in the ratio of grid number to the computing cores or due to an increase in the amount of data transferred between nodes. Decreasing the ratio of grid number to the computing cores reduces the computational time significantly compared to the nodes' data transfer time. Although Case C experienced the highest relative NCPL, it has shown the highest computing and parallelisation performance owing to its higher convergence and shorter execution time.

5. Conclusion

LES simulation was used to predict flow separation zones and separation effects on heat transfer in a three-dimensional diffuser employing dynamic Smagorinsky subgrid-scale model. Three grid arrangements were utilized to study the grid resolution effects on the near-wall LES results and the dimensionless parameters of the Case C were in an acceptable range. The velocity profiles and wall pressure distribution obtained for Case C were compared with those of DNS and experimental results and show good agreements. The pressure coefficient predicted for Case C showed a similar trend to those of the referenced results. It was shown that in most regions of the flow field, the TKE is resolved above 80%, which is one of the requirements of a high-quality near-wall LES calculations. The PSD was computed for two spots in the regions with the lowest grid resolution and it was shown that an acceptable energy cascade was achieved at those two points. Also, a probe was located at the recirculation zone to provide another view point for LES flow calculation in such region. The PSD diagrams imply that the LES calculation resolved large scales of flow, which control turbulent diffusion of momentum and heat. A finite volume solver was extended in OpenFOAM to solve energy equation for incompressible flow and a limiter was introduce to the solver to prevent non-physical heat transfer and numerical instability which may result from backscatter phenomena. The extended solver was validated by calculating flow in a three-dimensional channel and a backward-facing step, and the present numerical results were in a good agreement with DNS calculations. The present study showed that the heat transfer from the walls is significantly affected by the flow separation and reduced in most of the separated flow domain. This reduction is resulted from the low velocity and TKE in the separated flow within the boundary layer. In another view, the regions with low velocity and TKE play the role of a thermal isolating layer and consequently, reduce the heat transfer from the wall. In the re-attachment region, the temperature was reduced indicating an increase in heat transfer. This increase in heat transfer is the result of an increase in turbulence intensity near the re-attachment zone. Computational cost and performance analysis showed that increasing the number of computational cells in Case C increased the convergence rate of the solver and thus, reduced the computation time and cost. It was also shown that solving the energy equation did not have a significant effect on the execution time. It increased the relative NCPL due to increase of data transfer between the computational cores.

References

[1] H. Iacovides, M. Raisee, Recent progress in the computation of flow and heat transfer in internal cooling passages of turbine blades, International Journal of Heat and Fluid Flow 20 (1999) 320–328.

[2] S. Vakilipour, M. Habibnia, M. Sabour, R. Riazi, M. Mohammadi, Surface pressure characteristics of a highly loaded turbine blade at design and off-design conditions; a CFD methodology, Thermophysics and Aeromechanics 24 (2017) 469–482.

[3] B. Wu, X. Yang, Z. Liu, Z. Feng, Effects of novel turning vanes on pressure loss and tip-wall heat transfer in an idealized u-bend channel, International Communications in Heat and Mass Transfer 121 (2021) 105072.

[4] M. M. Ghorani, M. H. S. Haghighi, A. Riasi, Entropy generation minimization of a pump running in reverse mode based on surrogate models and nsga-ii, International Communications in Heat and Mass Transfer 118 (2020) 104898.

[5] C. Meyer, Numerical investigation of the effect of inlet flow distortions on forced draught air-cooled heat exchanger performance, Applied Thermal Engineering 25 (2005) 1634–1649.

[6] S. Vakilipour, S. Ormiston, A coupled pressure-based co-located finite-volume solution method for natural-convection flows, Numerical Heat Transfer, Part B: Fundamentals 61 (2012) 91–115.

[7] A. Abdon, B. Sundén, Investigation of a turbulence model for wall cooling of combustion chambers, in: ASME 1998 International Gas Turbine and Aeroengine Congress and Exhibition, American Society of Mechanical Engineers Digital Collection, 1998.

[8] S. Vakilipour, Y. Tohidi, J. Al-Zaili, R. Riazi, A numerical investigation of CO2 dilution on the thermochemical characteristics of a swirl stabilized diffusion flame, Applied Mathematics and Mechanics 41 (2020) 327–348.

[9] J. Alzaili, A. Sayma, Challenges in the development of micro gas turbines for concentrated solar power systems, in: 8th International Gas Turbine Conference, Brussels, Belgium, 2016.

[10] A. Sayma, D. Iaria, M. Khader, J. Al Zaili, Multi-objective optimisation of a centrifugal compressor for a micro gas turbine operated by concentrated solar power, in: Proceedings of the Global Power and Propulsion Forum 2017, 2017.

[11] T. Verstraete, Z. Alsalihi, R. Van den Braembussche, Numerical study of the heat transfer in micro gas turbines, Journal of turbomachinery 129 (2007) 835–841.

[12] R. Van den Braembussche, Z. Alsalihi, A. Islek, Aerothermal optimization of micro-gas turbine compressor including heat transfer, VKI, 2003.

[13] M. Darbandi, S. Vakilipour, Solution of thermally developing zone in short micro-/nanoscale channels, Journal of heat transfer 131 (2009).

[14] S. Vakilipour, M. Darbandi, Advancement in numerical study of gas flow and heat transfer in a microscale, Journal of Thermophysics and Heat Transfer 23 (2009) 205–208.

[15] M. Seyednia, M. Masdari, S. Vakilipour, Numerical assessment of a deformable trailing-edge flap on aerodynamic load

control of a pitching S809 airfoil using OpenFOAM, Proceedings of the Institution of Mechanical Engineers, Part A: Journal of Power and Energy 233 (2019) 890–900.

[16] E. M. Cherry, C. J. Elkins, J. K. Eaton, Geometric sensitivity of three-dimensional separated flows, International Journal of Heat and Fluid Flow 29 (2008) 803–811.

[17] L. R. Reneau, J. Johnston, S. J. Kline, Performance and design of straight, two-dimensional diffusers, Journal of Basic Engineering 89 (1967) 141–150.

[18] J. Ohlsson, P. Schlatter, P. F. Fischer, D. S. Henningson, Direct numerical simulation of separated flow in a three-dimensional diffuser, Journal of Fluid Mechanics 650 (2010) 307–318.

[19] S. Jakirlić, G. Kadavelil, M. Kornhaas, M. Schäfer, D. Sternel, C. Tropea, Numerical and physical aspects in les and hybrid les/rans of turbulent flow separation in a 3-d diffuser, International Journal of Heat and Fluid Flow 31 (2010) 820–832.

[20] K.-i. Abe, T. Ohtsuka, An investigation of les and hybrid les/rans models for predicting 3-d diffuser flow, International Journal of Heat and Fluid Flow 31 (2010) 833–844.

[21] K.-i. Abe, An investigation of sgs stress anisotropy modeling in complex turbulent flow fields, Flow, turbulence and combustion 92 (2014) 503–525.

[22] H. Togun, S. Kazi, A. Badarudin, A review of experimental study of turbulent heat transfer in separated flow, Australian Journal of Basic and Applied Sciences 5 (2011) 489–505.

[23] C. Oon, H. Togun, S. Kazi, A. Badarudin, E. Sadeghinezhad, Computational simulation of heat transfer to separation fluid flow in an annular passage, International communications in heat and mass transfer 46 (2013) 92–96.

[24] H. Togun, H. I. Abu-Mulaweh, S. N. Kazi, A. Badarudin, Numerical simulation of heat transfer and separation al2o3/nanofluid flow in concentric annular pipe, International Communications in Heat and Mass Transfer 71 (2016) 108–117.

[25] P. Durbin, Z. Yin, E. Jeyapaul, Adaptive detached-eddy simulation of three-dimensional diffusers, Journal of Fluids Engineering 138 (2016) 101201.

[26] H. Schneider, D. von Terzi, H.-J. Bauer, W. Rodi, Reliable and accurate prediction of three-dimensional separation in asymmetric diffusers using large-eddy simulation, Journal of Fluids Engineering 132 (2010) 031101.

[27] H. Steiner, S. Jakirlic, G. Kadavelil, R. Manceau, S. Saric, G. Brenn, 13th ERCOFTAC workshop on refined turbulence modelling, ERCOFTAC Bull 78 (2008) 22–27.

[28] J. Weatheritt, R. Sandberg, The development of algebraic stress models using a novel evolutionary algorithm, International Journal of Heat and Fluid Flow 68 (2017) 298–318.

[29] Z. Yin, P. A. Durbin, An adaptive des smodel that allows wall-resolved eddy simulation, International Journal of Heat and Fluid Flow 62 (2016) 499–509.

[30] Z. Yin, K. Reddy, P. A. Durbin, On the dynamic computation of the model constant in delayed detached eddy simulation, Physics of Fluids 27 (2015) 025105.

[31] E. Jeyapaul, Turbulent flow separation in three-dimensional asymmetric diffusers, Digital Repository@ Iowa State University, 2011.

[32] S. Jakirlić, R. Maduta, Extending the bounds of ‘steady’rans closures: Toward an instability-sensitive reynolds stress model, International Journal of Heat and fluid flow 51 (2015) 175–194.

[33] J. Kim, P. Moin, Transport of passive scalars in a turbulent channel flow, in: Turbulent Shear Flows 6, Springer, 1989, pp. 85–96.

[34] M. Niemann, J. Fröhlich, Direct numerical simulation of turbulent heat transfer behind a backward-facing step at low prandtl number, PAMM 14 (2014) 659–660.

[35] R. V. Avancha, R. H. Pletcher, Large eddy simulation of the turbulent flow past a backward-facing step with heat transfer

and property variations, International Journal of Heat and Fluid Flow 23 (2002) 601–614.

[36] M. Lesieur, O. Metais, New trends in large-eddy simulations of turbulence, Annual review of fluid mechanics 28 (1996) 45–82.

[37] J. Smagorinsky, General circulation experiments with the primitive equations: I. the basic experiment, Monthly weather review 91 (1963) 99–164.

[38] M. Germano, U. Piomelli, P. Moin, W. H. Cabot, A dynamic subgrid-scale eddy viscosity model, Physics of Fluids A: Fluid Dynamics 3 (1991) 1760–1765.

[39] D. K. Lilly, A proposed modification of the germano subgrid-scale closure method, Physics of Fluids A: Fluid Dynamics 4 (1992) 633–635.

[40] M. Lesieur, O. Métais, P. Comte, et al., Large-eddy simulations of turbulence, Cambridge university press, 2005.

[41] U. Piomelli, W. H. Cabot, P. Moin, S. Lee, Subgrid-scale backscatter in turbulent and transitional flows, Physics of Fluids A: Fluid Dynamics 3 (1991) 1766–1771.

[42] F. Nicoud, H. B. Toda, O. Cabrit, S. Bose, J. Lee, Using singular values to build a subgrid-scale model for large eddy simulations, Physics of Fluids 23 (2011) 085106.

[43] M. Baba-Ahmadi, G. Tabor, Inlet conditions for les using mapping and feedback control, Computers & Fluids 38 (2009) 1299–1311.

[44] A. Montorfano, F. Piscaglia, G. Ferrari, Inlet boundary conditions for incompressible les: A comparative study, Mathematical and Computer Modelling 57 (2013) 1640–1647.

[45] S. Rezaeiravesh, M. Liefvendahl, Effect of grid resolution on large eddy simulation of wall-bounded turbulence, Physics of Fluids 30 (2018) 055106.

[46] J. Kim, P. Moin, R. Moser, Turbulence statistics in fully developed channel flow at low reynolds number, Journal of fluid mechanics 177 (1987) 133–166.

[47] W.-P. Wang, R. H. Pletcher, On the large eddy simulation of a turbulent channel flow with significant heat transfer, Physics of Fluids 8 (1996) 3354–3366.

[48] N. Kasagi, A. Matsunaga, Three-dimensional particle-tracking velocimetry measurement of turbulence statistics and energy budget in a backward-facing step flow, International journal of heat and fluid flow 16 (1995) 477–485.

[49] S. B. Pope, Turbulent flows, IOP Publishing, 2001.

[50] A. Keating, U. Piomelli, K. Bremhorst, S. Nešić, Large-eddy simulation of heat transfer downstream of a backward-facing step, Journal of Turbulence 5 (2004) 020.

[51] J. Vogel, J. Eaton, Combined heat transfer and fluid dynamic measurements downstream of a backward-facing step (1985).